RSC Advances

PAPER

View Article Online
View Journal | View Issue

Cite this: *RSC Adv.*, 2026, **16**, 18679

Fabrication of methotrexate conjugated multi-walled carbon nanotubes for the evaluation of cytotoxic potential at biochemical and molecular level modulating *BAX*, *BCL-2* and telomerase expression

Harshita Tiwari,[a] Swati Singh,[a] Vandana Kumari,[a] Shikha Tripathi,[b] Anurag Kumar Singh,[c] Avanish Singh Parmar,[b] Santosh Kumar Singh[a] and Vibhav Gautam *[a]

Cancer is one of the leading causes of mortality all across the world, and the clinical applications of numerous chemotherapeutic agents are limited by major side effects. Among these, methotrexate (MTX) is a widely used anticancer drug which exhibits certain limitations related to biocompatibility and solubility. Therefore, to address these limitations, MTX was covalently conjugated to multi-walled carbon nanotubes (MWCNTs) to develop a stable and targeted nanotherapeutic system. MWCNTs were first subjected to purification followed by carboxylation which was validated through dispersion solubility test. MTX-MWCNT was then subjected to characterization to validate successful conjugation after which the cytotoxic potential of MTX-MWCNT was assessed by cell viability assay on MCF-7 (hormone-positive breast cancer), MDA-MB 231 (triple-negative breast cancer), and HeLa (cervical cancer) cells. The evaluation of safety profile and hemocompatibility was done using non-cancerous HEK 293T (human embryonic kidney) cells and *in vitro* hemolysis assay respectively. The cytotoxic potential of MTX-MWCNT was assessed through cell viability assay which demonstrated a dose-dependent reduction in cancer cell viability after treatment with MTX-MWCNTs with minimal toxicity toward normal cells and blood. The anti-angiogenic potential of MTX-MWCNT was also tested further through *ex vivo* chick chorioallantoic membrane (CAM) assay which revealed significant reduction in vessel branching. The cytotoxic activity of MTX-MWCNT was also confirmed by biochemical assays, including cell proliferation assay, glucose estimation assay, and total antioxidant status (TAS). Moreover, the cytotoxic potential of MTX-MWCNT was further assessed at the gene level through quantitative reverse transcription polymerase chain reaction (qRT-PCR) analysis which demonstrated upregulation of the pro-apoptotic *BAX* gene and downregulation of the anti-apoptotic *BCL-2* gene. Furthermore, kit-based enzyme-linked immunosorbent assay (ELISA) quantification further confirmed increased *BAX*, decreased *BCL-2*, and reduced telomerase protein expression. Lastly, the alteration in nuclear morphology in all three cancer cells post treatment with MTX-MWCNTs was evaluated through 4′,6-diamidino-2-phenylindole (DAPI) staining followed by fluorescence microscopy. Collectively, the obtained findings highlight that MTX-MWCNT efficiently induces apoptosis and inhibits angiogenesis while maintaining significant biosafety, establishing it as an emerging nanoscale platform for targeted cancer therapy.

Received 16th November 2025
Accepted 16th March 2026

DOI: 10.1039/d5ra08838k

rsc.li/rsc-advances

1. Introduction

Cancer continues to be a major global health challenge, estimating an increase to 29.9 million new cases and 15.3 million mortalities projected by 2040.[1] Despite significant advancements in early detection and therapeutic modalities, the complexity and heterogeneity of cancer cells still remain the leading challenges in achieving effective and sustained therapeutic outcomes. Conventional therapies, including chemotherapy, radiotherapy, and surgery, often face limitations such as systemic toxicity, multidrug resistance, and off-site targeting, due to which the

[a]*Centre of Experimental Medicine and Surgery, Institute of Medical Sciences, Banaras Hindu University, Varanasi 221005, Uttar Pradesh, India. E-mail: vibhav.gautam4@bhu.ac.in; harshitatiwari@bhu.ac.in; swati.7672@bhu.ac.in; vandana.biotech04@gmail.com; santosh.singh01@bhu.ac.in; Tel: +918860182113*

[b]*Department of Physics, Indian Institute of Technology (BHU), Varanasi 221005, Uttar Pradesh, India. E-mail: shikha.rs.phy22@itbhu.ac.in; asparmar.phy@itbhu.ac.in*

[c]*Department of Pharmaceutical Engineering and Technology, Indian Institute of Technology (BHU), Varanasi 221005, Uttar Pradesh, India. E-mail: anuragvcp@gmail.com*

development of innovative therapeutic strategies is highly required. Nanotechnology has revolutionized the biomedical sector by offering novel and unique platforms for drug delivery and therapeutic interventions, particularly in cancer treatment. Nanocarriers offer unique advantages such as improved pharmacokinetic profiles, enhanced solubility, controlled release, selective targeting, and precise diagnosis.[2] These properties are often exploited in cancer therapeutics because conventional chemotherapeutic drugs often face challenges including systemic toxicity, non-specific distribution, rapid clearance, and poor bioavailability, leading to suboptimal therapeutic outcomes and severe side effects.[3] For example, recent studies have reported that doxorubicin induces significant cardiotoxicity even at clinically relevant doses resulting in long-term cardiac dysfunction in cancer patients.[4] Similarly, cisplatin has also been reported to display renal toxicity, often necessitating dose reduction and compromising therapeutic efficacy.[5] MTX, another widely used chemotherapeutic agent, has also been reported to cause hepatotoxicity and gastrointestinal toxicity, which significantly affect patient compliance and treatment outcomes.[6] These adverse effects highlight the pressing need for advanced drug delivery systems capable of enhancing therapeutic efficacy and improved biocompatibility. Among these chemotherapeutic agents, MTX stands out as a widely used drug with significant anticancer and immunosuppressive potential.

MTX is a well-known chemotherapeutic drug and folic acid antagonist that blocks DNA replication by inhibiting the activity of the enzyme dihydrofolate reductase crucial for the synthesis of purines and pyrimidines. It has been widely used for the treatment of various malignancies including breast, lung, leukaemia, head and neck.[7] However, the drug has various adverse effects such as hepatotoxicity, teratogenic effects, bone marrow suppression, and inflammation, which are often dose-dependent and require dose adjustments to minimize toxicity while maintaining therapeutic efficacy.[8,9] Various nanocarriers such as polymeric NPs, dendrimers, metallic nanoparticles (NPs), carbon nanotubes (CNTs), lipid-based NPs and magnetic NPs have been used for conjugation with MTX to enhance its targeted delivery and reduce the toxicity.[10] Among wide range of nanomaterials, MWCNTs have been exploited due to their physio-chemical attributes, thermal conductivity and chemical stability. MWCNTs are well arranged cylindrical structures of graphene layers that have emerged as novel candidates for their applications in biomedical field due to their versatility. MWCNTs are generally preferred over single-walled carbon nanotubes (SWCNTs) due to larger surface area and higher tensile strength. Multiple researches on the functionalization and applications of MWCNTs have been performed in recent years. Several different types of drugs and biomolecules can be conjugated with MWCNTs because of their opto-electronic, structural and mechanical properties.[11] The conjugation of any therapeutic agent with MWCNTs has been made possible by subjecting them to chemical modifications. For example, in a recent work, researchers demonstrated the effectiveness of using functionalized MWCNTs as a vehicle for efficient co-delivery of curcumin and MTX in cancer therapeutics, highlighting the potential of MWCNTs in combination therapies.[12]

The present study focuses on the synthesis and characterization of MTX conjugated with MWCNTs. In this study, MWCNTs were first carboxylated to introduce carboxyl groups, which were subsequently used for covalent conjugation with MTX through amide bond formation. The resulting MTX-MWCNT nanoconjugate was characterized using spectroscopic and microscopic techniques to confirm successful functionalization and conjugation. In this study, MCF-7, MDA-MB-231, and HeLa cells were selected as representative models to evaluate the anticancer potential of MTX-MWCNTs. MCF-7 cells are widely used as a model of hormone receptor-positive breast carcinoma, whereas MDA-MB 231 cells represent triple-negative breast cancer which is a highly aggressive and metastatic subtype.[13] HeLa cells, derived from cervical carcinoma, were also included additionally to assess the broader applicability of the nanoconjugates across different cancer types. Apart from these, HEK 293T cells were used as representative model for non-cancerous cells for the evaluation of safety profile of MTX-MWCNTs. After thorough characterization, the synthesized nanoconjugate was evaluated for its cytotoxic potential through cell viability, cell proliferation and biochemical assays, followed by evaluation of hemocompatibility and anti-angiogenic activity. Furthermore, qRT-PCR was also employed for the analysis of differential expression of pro-apoptotic (*BAX*) and anti-apoptotic (*BCL-2*) genes followed by kit-based sandwich ELISA assays to quantify relevant levels of BAX, BCL-2 and telomerase proteins. Lastly, DAPI staining was performed to study morphological alteration in nucleus employing fluorescence microscopy. While previous studies have explored MTX conjugation to MWCNTs, our method involving carboxylation followed by amide bond formation is reported here for the first time. The combination of cell viability assay, *in vitro* hemolysis assay, *ex vivo* CAM assay, DAPI staining-based fluorescence microscopy, biochemical assays including cell proliferation analysis, glucose estimation and TAS, along with detailed gene and protein analyses at molecular level across diverse cancer cell lines (MCF-7, MDA-MB 231, and HeLa), has also been performed for the first time. This study highlights the novelty of our approach, and the synthesized nanoconjugate demonstrates significant potential as a targeted nanocarrier for cancer therapy.

2. Experimental section

2.1 Materials

Raw MWCNTs (purity: >98%, length: 2.5–20 μm, diameter: 6–13 nm), *N*-hydroxysuccinimide (NHS), dicyclohexylcarbodiimide (DCC) and gene-specific primers were purchased from Sigma Aldrich, USA. MTX (98%), 3-(4,5-dimethylthiazol-2-yl)-2,5-diphenyltetrazolium bromide (MTT), dimethyl sulphoxide (DMSO) (99.5%), trypan blue, crystal violet and Bradford reagent were purchased from SRL, India. DAPI staining solution was purchased from Puregene, Genetix. HPLC grade water was obtained from Merck, Germany. Hydrochloric acid (HCl), sulfuric acid (H_2SO_4), nitric acid (HNO_3), methanol and absolute ethanol of analytical grade were used for the experiments. Trypsin-ethylenediaminetetraacetic acid (trypsin-EDTA),

Dulbecco's Modified Eagle Medium (DMEM), bovine serum albumin (BSA) and phosphate buffer saline (PBS) were purchased from Himedia, India. Antibiotic–antimycotic solution containing penicillin, amphotericin B, and streptomycin was obtained from Cell Clone, India. Fetal bovine serum (FBS) and PowerUp SYBR Green master mix were procured from Thermo Fisher Scientific, USA. The human cell lines MCF-7, MDA-MB 231, HeLa and HEK 293T were procured from National Centre for Cell Science (NCCS), Pune, India.

2.2 Methodology

2.2.1 Synthesis of MTX-MWCNT

2.2.1.1 Purification of raw MWCNTs. Acidic purification of raw MWCNTs (r-MWCNTs) was done through a non-oxidative approach to remove the impurities and amorphous carbon. Briefly, 500 mg of r-MWCNTs were dissolved in 10 mL of 20% HCl followed by 20 minutes sonication with repeated swirling. The dispersion was subjected to magnetic stirring at room temperature for 24 hours. After 24 hours, MWCNTs were filtered and rinsed with deionized water and the process was repeated until neutral pH was maintained. The neutralized MWCNTs were then filtered and were kept in oven until completely dried.[14] The purified MWCNTs (p-MWCNTs) were ready for further use.

2.2.1.2 Carboxylation of purified MWCNTs. The carboxylation of p-MWCNTs was done through an oxidative approach in which HNO_3 and H_2SO_4 were mixed in 1 : 3 ratio to prepare 100 mL of mixture. 400 mg of p-MWCNTs were added to the prepared acidic mixture followed by 2 hours of sonication with repeated swirling. The dispersion was then subjected to magnetic stirring at room temperature for 24 hours. After 24 hours, 400 mL of deionized water was added and left overnight on magnetic stirrer and then filtered. This process was repeated till neutrality after which c-MWCNTs were filtered and kept in oven until completely dried.[15] The carboxylated MWCNTs (c-MWCNTs) were now ready for conjugation with MTX.

2.2.1.3 Conjugation of carboxylated MWCNTs with MTX. Briefly, 100 mg of c-MWCNTs, 720 mg DCC and 400 mg NHS were dissolved in 20 mL DMSO and allowed to react for 48 hours at room temperature in dark under nitrogenous environment. After 48 hours, dicyclohexylurea was produced as precipitate which was filtered to obtain pure MWCNT-NHS. 60 mg of MTX was then added to the produced MWCNT-NHS and the reaction mixture was sonicated for 10 minutes at room temperature after which it was allowed to react in dark for 48 hours. 100 mL of deionized water was then added to the reaction mixture to precipitate MTX-MWCNT conjugate which was then filtered and was allowed to dry in oven.[16]

2.2.2 Characterization of MTX-MWCNTs

2.2.2.1 Dispersion solubility test. The preliminary confirmation of the carboxylation of MWCNTs was done by the dispersion solubility test. Briefly, 5 mg each of r-MWCNTs, p-MWCNTs and c-MWCNTs were dispersed in 5 mL deionized water and each mixture was sonicated for 10 minutes. The dispersions were left undisturbed for 30 days and the images were captured at 0 hours, after 1 day, 7 days and 30 days.[17]

2.2.2.2 Fourier transform infra-red (FTIR) spectroscopy. FTIR analysis of r-MWCNTs, p-MWCNTs, c-MWCNTs, MTX and MTX-MWCNT was done after preliminary characterization to confirm the presence of characteristic functional groups corresponding to the chemical modification. The samples were prepared in the form of KBr pellets after which the FTIR spectra were recorded in the range of 500–4000 cm^{-1} using PerkinElmer FT-IR spectrophotometer.

2.2.2.3 Raman spectroscopy. Raman spectra were recorded for the analysis of functional properties of the synthesized nanoconjugate using Raman spectroscopy (WITec, Oxford Instruments, Alpha 300 RS Model). The spectrophotometer was operated at an excitation wavelength of 532 nm for p-MWCNTs and MTX-MWCNTs while for MTX, the excitation wavelength was increased to 785 nm to observe the spectra. The operating power for p-MWCNTs and MTX-MWCNTs was in the range of 2–5 mW while for MTX, the operating power was 40 mW.

2.2.2.4 X-ray photoelectron spectroscopy (XPS). XPS analysis was done for the elemental analysis of the synthesized nanoconjugate and it was executed by using XPS spectrophotometer (Thermo Fisher Scientific, K-Alpha Model) which is equipped with a monochromatic K-Alpha radiation source. Carbon 1s peak at 284.5 eV was used as internal standard for calibration and identification of characteristic binding energies. XPS peak fitting software was used for recording the data by the aid of energy at 93.3 eV at room temperature and under ultra-high vacuum conditions.

2.2.2.5 Transmission electron microscopy (TEM). Transmission Electron Microscopy (TEM) was performed for the analysis of two-dimensional (2D) morphology of the synthesized nanoconjugate. The samples were dissolved in absolute ethanol and a drop of this solution was placed on a carbon grid after which it was subjected to drying at room temperature. The images were captured using a transmission electron microscope (Tecnai G220 S-TWIN TEM) at an accelerating voltage of 200 kV. At last, the average diameter was measured using Image J software.

2.2.2.6 Field emission scanning electron microscopy (FE-SEM). Field Emission Scanning Electron Microscopy (FE-SEM) imaging was to used analyze the three-dimensional (3D) morphology and the surface topology of the synthesized nanoformulation using a field emission scanning electron microscope (Carl Zeiss, Gemini 560). The dried nanotubes were placed on a carbon tape and subjected to imaging at an accelerating voltage of at 100k× magnification. The average diameter was then measured using Image J software.

2.2.2.7 Dynamic light scattering (DLS) and zeta potential. Zeta potential and poly dispersity index (PDI) were analyzed using a Zeta Sizer Ultra ZSU5700 instrument (Malvern Panalytical, UK). The synthesized nanoconjugates were dispersed in deionized water followed by brief sonication. The phenomena of angular DLS and electrophoretic light scattering were used for recording the PDI and zeta potential respectively.

2.2.3 Evaluation of cytotoxic potential of MTX-MWCNTs

2.2.3.1 Cell growth and maintenance. DMEM supplemented with 10% heat-inactivated FBS and 1% antibiotic-antimycotic solution was used to culture MCF-7, MDA-MB 231, HeLa and

HEK 293T cells. The cells were maintained in healthy condition at 37 °C in 5% CO_2 incubator (Panasonic, Sakata, Japan). The cells were allowed to proliferate until 80–90% confluency of adherent monolayer cells was attained and were observed regularly for any contamination or morphological change.

2.2.3.2 Cell viability assay. The cytotoxic activity was assessed using MTT assay to calculate IC_{50} value which is the minimum concentration of the compound required for 50% cell death. The adherent cells were harvested after attaining sub-confluency using trypsin for clearing the adherence. The harvested cells were stained using trypan blue followed by counting using hemocytometer. 1×10^4 cells per well were seeded in a 96-well plate and were allowed to adhere overnight at 37 °C in 5% CO_2 incubator. For cytotoxicity evaluation, both MTX and MTX-MWCNT were initially dissolved in 0.1% (v/v) DMSO and further diluted with complete culture medium to the desired concentrations. The final DMSO concentration in all wells was maintained at 0.1%, which is non-toxic to cells.[18] MTX-treated cells were used as the positive control, while cells receiving only culture medium containing 0.1% DMSO served as the vehicle control. After the cells were adhered, they were treated with different concentrations of MTX-MWCNTs and MTX (5, 10, 25, 50, 100, 150 and 200 μg mL^{-1}) and incubated at 37 °C in 5% CO_2 incubator for 24 hours. After 24 hours of incubation, 10 μL of 5 mg mL^{-1} MTT dissolved in 1X PBS was added to each well followed by 4 hours of incubation. The plate was then centrifuged at the rate of 3000 rpm for 20 minutes after which the supernatant was discarded. 100 μL of DMSO was then added to each well to dissolve the pelleted formazan crystals properly by rigorous pipetting. After the violet-coloured formazan crystals were completely dissolved, the absorbance was recorded using a microplate reader (Thermo Fisher Scientific) at 570 nm.[19] The percentage cell viability was calculated using the formula:

$$\%\ \text{cell viability} = (OD_{(570)}\ \text{of treated cells}/OD_{(570)}\ \text{of control cells}) \times 100$$

2.2.3.3 In vitro hemolysis assay. After the investigation of cytotoxicity, the hemolysis assay was performed to determine the action of MTX-MWCNTs on RBCs for the evaluation of its hemocompatibility. The experiment has been approved by Institutional Ethics Committee, Institute of Medical Sciences, Banaras Hindu University, Varanasi under the approval letter number IMS/IEC/2025/7913 and informed consent was obtained from all donors. Fresh blood from healthy donors was collected in citrate tube through venipuncture after which the blood sample was subjected to centrifugation at the rate of 1500 rpm for 10 minutes for harvesting the RBCs. The harvested RBCs were washed with 1× PBS thrice after which they were finally suspended in PBS. The collected RBCs were treated with different concentrations of MTX-MWCNTs (5, 10, 25, 50, 100, 200, 500 and 1000 μg mL^{-1}). RBCs suspended in 0.1% DMSO in 1× PBS were used as vehicle control, while RBCs suspended in 1× Triton X-100 were used as positive control. The complete reaction mixture was then incubated in an oscillator at the rate of 600 rpm for 3 hours at 37 °C. The RBCs were then subjected to centrifugation at the rate of 8000 rpm for 5 minutes following which the supernatant was transferred to a 96 well plate.[20] At last, the absorbance was recorded at 540 nm and the percentage hemolysis was calculated using the formula:

$$\%\ \text{hemolysis} = (OD_{(540)}\ \text{of sample} - OD_{(540)}\ \text{of negative control})/(OD_{(540)}\ \text{of positive control} - OD_{(540)}\ \text{of negative control}) \times 100$$

The microscopic visualization of the RBCs was done subsequently using bright-field microscope (Olympus, CX43, Tokyo, Japan) at 100× magnification with 10 μm scale bar.

2.2.3.4 Ex vivo chorioallantoic membrane (CAM) assay. After the evaluation of cytotoxic potential and safety profile, the *ex vivo* CAM assay was conducted to assess the anti-angiogenic potential of the synthesized nanoformulation. Briefly, fertilized chicken eggs were procured and incubated at 37 °C under humid conditions. After seven days of incubation, a square window was aseptically created on each egg. The CAM was then treated with different concentrations of MTX-MWCNT (10, 25, 50, and 100 μg mL^{-1}). MTX-MWCNTs were dissolved in 0.1% DMSO diluted with 1× PBS to the desired concentrations. MTX (10 μg mL^{-1}) and 0.1% DMSO in 1× PBS served as positive and vehicle controls, respectively. The windows were subsequently sealed with parafilm, and photographs of the CAM were captured after 0, 24, and 48 hours of treatment for macroscopic evaluation of vessel branching and effect on angiogenesis. Furthermore, the quantification of the vascular parameters including total vessel length, number of branching points, number of junctions and vessel thickness was also performed after 0 and 48 hours of incubation using FIJI (Image J) software.

2.2.3.5 Investigation of cell proliferation. Cell proliferation assay was further performed to examine the percentage cell proliferation of cancer cells post treatment with MTX-MWCNTs at IC_{50} concentration using crystal violet stain. Briefly, 1×10^4 cells per well were seeded in a 96-well plate and were allowed to incubate overnight at 37 °C in 5% CO_2 incubator. After 24 hours, the cells were given treatment with vehicle control (0.1% DMSO in culture medium) and IC_{50} concentration of MTX-MWCNTs and MTX. After next 24 hours of treatment, the existing media was discarded to proceed further. The cells were then allowed to fix for 10 minutes in absolute ethanol. After fixation, the cells were stained with 0.05% crystal violet in 20% ethanol and were allowed to incubate for 10 minutes. After incubation, the cells were rinsed with distilled water and the formed crystals were solubilized using methanol. At last, the absorbance was recorded at 595 nm and percentage cell proliferation was calculated using the formula:

$$\%\ \text{cell proliferation} = (OD_{(595)}\ \text{of treated cells}/OD_{(595)}\ \text{of control cells}) \times 100$$

2.2.3.6 Estimation of glucose uptake. Cancer cells often prioritize increased glucose uptake through aerobic glycolysis for enhanced cell proliferation. Therefore, after examining the effect of MTX-MWCNT on cell proliferation, glucose estimation

was done for the evaluation of alteration in glucose uptake of cancer cells post treatment with MTX-MWCNTs at IC_{50} concentration. 0.1% DMSO in cell culture medium was used as vehicle control, while MTX at IC_{50} concentration was used as positive control. The assay was performed using glucose estimation kit from Beacon Diagnostics, India as per the manufacturer's protocol and the absorbance of control cells and treated cells was recorded at 505 nm. The concentration of unconsumed glucose content in the media was calculated in mg dl^{-1} using a reference standard of known concentration provided in the kit and the data was analyzed statistically. The concentration of glucose in media was calculated using the formula:

$$\text{Glucose concentration (mg dl}^{-1}\text{)} = (\text{OD}_{(505)} \text{ of sample}/\text{OD}_{(505)} \text{ of standard}) \times 100$$

2.2.3.7 Determination of total antioxidant status (TAS). Total antioxidant assay was performed for the determination of oxidative stress-mediated apoptosis of the cells after treatment. Briefly, after treatment with vehicle control (0.1% DMSO in cell culture medium) and IC_{50} concentrations of MTX-MWCNTs and MTX for 24 hours, cell culture supernatants were harvested and used for analysis according to the manufacturer's instructions. The TAS of treated cells was determined from the harvested cell culture supernatants using a colorimetric ABTS kit from Elabscience. The absorbance was recorded at 660 nm to calculate TAS using the obtained standard curve (Fig. S4A) and the results were expressed in mmol Trolox equiv. per L.

2.2.3.8 Differential expression of BAX and BCL-2 genes using qRT-PCR. After the investigation of cytotoxicity at biochemical level, the cytotoxic potential of MTX-MWCNTs was further validated at molecular level by analysing the relative expression level of pro-apoptotic (*BAX*) and anti-apoptotic (*BCL-2*) gene using qRT-PCR (QuantStudio 5 Real-Time PCR System, Thermo Fisher Scientific, USA) according to the MIQE guidelines.[21] The cancer cells were seeded and were allowed to attain 80% confluency after which they were treated with vehicle control (0.1% DMSO in cell culture medium) and IC_{50} concentrations of MTX-MWCNTs and MTX. After 24 hours, total RNA was isolated from vehicle control and treated cells using total RNA isolation kit (Thermo Fisher Scientific, USA). The purity and the concentration of the isolated RNA were determined using NanoDrop (Thermo Scientific, USA). 2 μg RNA from each group was subjected to reverse transcription using High-Capacity cDNA Reverse Transcription Kit (Thermo Fisher Scientific, USA) for synthesizing the respective cDNA as per the manufacturer's protocol. qRT-PCR was then performed using gene-specific primers (Table S2), PowerUp SYBR Green Master Mix and the synthesized cDNA as template. *18s* gene was used as an endogenous control for normalization and the calculation of ΔC_T values. The difference between the ΔC_T values of vehicle control and treated samples ($\Delta\Delta C_T$) was then calculated and the relative gene expression levels corresponded to the calculated fold change values determined using $2^{-\Delta\Delta C_T}$ method. The results are presented as the mean of two independent experiments, with each sample analyzed in triplicate across three data sets.

2.2.3.9 Quantification of BAX, BCL-2 and telomerase protein levels using sandwich ELISA. After the evaluation of cytotoxicity at gene level, sandwich ELISA assay was further performed to validate the expression of BAX, BCL-2 and telomerase protein levels in cell extracts after treatment with MTX-MWCNTs at IC_{50} concentration. The cancer cells were seeded and treated with vehicle control (0.1% DMSO in cell culture medium) and IC_{50} concentrations of MTX-MWCNTs and MTX after which they were harvested using trypsinization. The harvested cells were then washed thrice using 1× PBS and were resuspended in it. The resuspended cells were then subjected to probe sonication and repeated freeze–thaw process for disruption of cell membrane and protein extraction. The supernatant in the form of cell lysate was then collected and proceeded for ELISA. The concentration of the harvested protein was determined using the Bradford assay, in which the absorbance of each sample was measured and compared against a standard curve prepared using known concentrations of BSA. The protein levels of BAX, BCL-2 and telomerase were quantified using Human ELISA Kits (Elabscience) as per the provided manufacturer's protocol. Briefly, each assay is based on colorimetric sandwich ELISA in which the absorbance measured at 450 nm is proportional to the analyte concentration. The standard curve was generated using the standards provided with each kit, which were subsequently applied to calculate the concentrations of BAX (Fig. S4B), BCL-2 (Fig. S4C) and telomerase (Fig. S4D) (ng mL^{-1}) in the test samples.

2.2.3.10 Evaluation of alteration in nuclear morphology using DAPI staining. The alteration in nuclear morphology of cancer cells after treatment was evaluated using DAPI staining. Briefly, 1×10^5 cells were seeded onto sterile coverslips placed in 6-well culture plates and allowed to attach overnight under standard culture conditions. After achieving appropriate confluency, the cells were treated with vehicle control, MTX-MWCNT and MTX at their respective IC_{50} concentrations. After 24 hours, the cells were washed twice with PBS and fixed with 4% paraformaldehyde for 15 minutes at room temperature. The fixed cells were again washed with PBS and were then permeabilized with 0.1% Triton X-100 for 5 minutes to facilitate nuclear dye penetration. The permeabilized cells were again subjected to PBS washing and subsequently incubated with DAPI solution (1 μg mL^{-1}) for 10 minutes in dark to stain the nuclear DNA. Excess stain was removed by washing with PBS, and the images were captured under a fluorescence microscope (Leica, Germany) to evaluate nuclear morphological alterations.

2.2.3.11 Statistical analysis. All experiments were performed in triplicates, and the data are presented as the mean ± SEM. The IC_{50} values were calculated using GraphPad Prism 8.0.2 by interpolation of the experimental data. One-way analysis of variance (one-way ANOVA) followed by Dunnett's multiple comparisons test was applied to analyze cell viability, *in vitro* hemolysis and sandwich ELISA data. The data of biochemical assays and qRT-PCR was analyzed by two-way ANOVA followed by Dunnett's and Tukey's multiple comparison tests respectively.[22] Statistical significance is indicated in each graph

relative to the vehicle control, with $p < 0.05$ represented as *, $p < 0.01$ as **, $p < 0.001$ as ***.

3. Results and discussion

3.1 Dispersion solubility test in aqueous medium confirmed the carboxylation of p-MWCNTs

The dispersibility of r-MWCNTs, p-MWCNTs and c-MWCNTs was evaluated through a sedimentation experiment in which it was observed that c-MWCNTs get easily dispersed in a polar solvent such as water as compared to r-MWCNTs and p-MWCNTs. The sedimentation of r-MWCNTs and p-MWCNTs started within few hours which pertains to their ability to agglomerate in aqueous solvents because of their high surface energy and weaker affinity with the dispersing solvent.[23] On the other hand, as observed in Fig. S1, c-MWCNTs remain well dispersed in water even after 30 days of dispersion. The underlying reason behind this is the presence of carboxyl and hydroxyl groups on the outer walls of c-MWCNTs that result in the formation of stronger hydrogen bonds with water than the existing weaker van der Waals interactions among MWCNTs.[24] Therefore, the oxidation of MWCNTs results in their improved dispersibility in polar solvents making them a suitable candidate to be conjugated with the target drug.

3.2 Fourier transform infrared (FTIR) spectroscopy analysis

FTIR of r-MWCNTs, p-MWCNT, c-MWCNTs and MTX-MWCNTs revealed the presence of characteristic functional groups corresponding to the functionalization (Fig. 1A). In r-MWCNTs and p-MWCNTs, peaks at 3446 cm^{-1} and 3449 cm^{-1} are attributed to O–H stretching vibrations respectively.[25] Furthermore, the characteristic peaks at 1459 cm^{-1} and 1556 cm^{-1} are attributed to C=C stretching in r-MWCNTs and p-MWCNTs respectively.[26] Two sharp peaks in the region of 2800 cm^{-1} and 3000 cm^{-1} are attributed to C–H bond stretching of inside surface of r-MWCNTs and p-MWCNTs.[27] However, these peaks appear sharper in case of c-MWCNTs due to strong aliphatic C–H stretching vibrations and acidic functionalization.[28] In case of c-MWCNTs, characteristic peaks at 1734 cm^{-1}, 1117 cm^{-1} and 1641 cm^{-1} corresponds to C=O, C–O and C=C stretching bands respectively indicating possible carboxylation.[29] In native MTX, strong peaks at 3411 cm^{-1} and 1646 cm^{-1} are attributed to N–H bending and C=O stretching vibrations respectively.[30] Peaks in the region of 1600 cm^{-1} and 1500 cm^{-1} corresponds to C=C stretching vibrations and C–N vibrations of the aromatic ring respectively.[30] Furthermore, peaks in the region of 1450 cm^{-1} and 1208 cm^{-1} are attributed to C–C and C–H bonds stretching vibrations.[30] The FTIR spectra of MTX-MWCNT conjugate was almost same as the native MTX with some minor changes incorporated due to its conjugation with MWCNTs. Here, in this case, conjugation is most probably expected by the formation of amide bond between MTX and f-MWCNT.[12] Peak shift from 1646 cm^{-1} to 1773 cm^{-1} in MTX-MWCNT is attributed to C=O stretching vibrations of the amide bond.[31] Furthermore, peaks shift at 1574 cm^{-1}, 1437 cm^{-1} and 1160 cm^{-1} and 1088 cm^{-1} are attributed to N–H

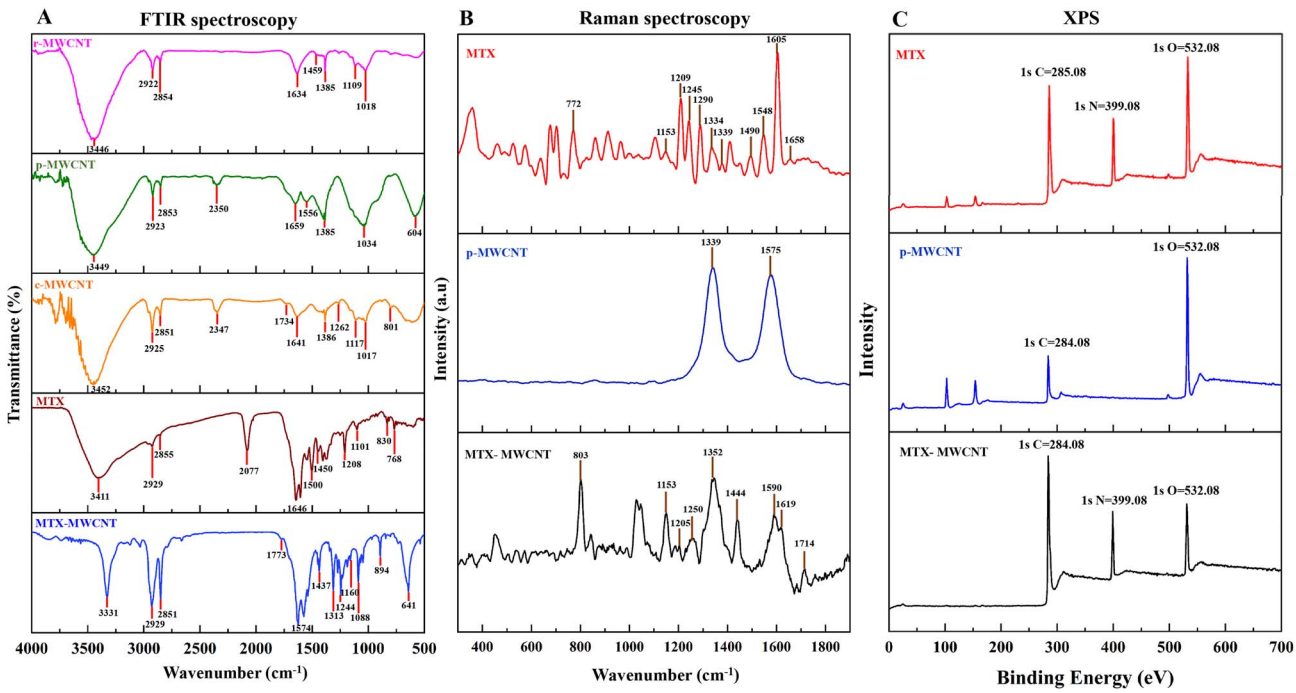

Fig. 1 Spectroscopy-based characterization of MWCNTs, MTX, and MTX-MWCNT conjugate. (A) FTIR spectra of r-MWCNT, p-MWCNT, c-MWCNT, MTX, and MTX-MWCNT nanoconjugate revealing the presence of characteristic functional groups. (B) Raman spectra MTX, p-MWCNTs and MTX-MWCNT nanoconjugate highlighting the D and G bands of CNTs along with the additional peaks corresponding to MTX, indicating successful conjugation. (C) XPS spectra of MTX, p-MWCNT, and MTX-MWCNT nanoconjugates displaying binding energies of C 1s, N 1s, and O 1s regions, further confirming drug attachment onto MWCNTs.

and C–N bending and stretching vibrations respectively.[32] Moreover, the rise in intensity of the dual peaks in the region between 2800 cm^{-1} and 3000 cm^{-1} of MTX-MWCNT as compared to r-MWCNTs also corresponds to the conjugation of MWCNT with MTX.[28]

3.3 Raman spectroscopy analysis

Raman spectroscopy-based characterization was done for the analysis of lattice structure and vibrational properties of p-MWCNTs and MTX-MWCNTs (Fig. 1B). The two prominent central peaks at 1339 cm^{-1} and 1575 cm^{-1} in p-MWCNTs reflects D band and G band respectively.[33] On the other hand, the peak shift of D and G band in MTX-MWCNTs was observed at 1352 cm^{-1} and 1590 cm^{-1} respectively due to drug conjugation. The D band is attributed to the heteroatomic structure, pentagonal–heptagonal pairs, vacancies among the tubular walls of MWCNTs and presence of impurities. Beside this, the G band corresponds to the tangential intraplanar vibrations among sp^2 graphitic carbon atoms.[34] The intensities of D band and G band (I_D/I_G) ratio is used to determine the degree of lattice defects in carbonaceous materials. The I_D/I_G ratio of p-MWCNTs and MTX-MWCNTs conjugate was found to be 1.007 and 1.0005 respectively. This lowering of the I_D/I_G ratio is due to the conjugation of the drug MTX with the functionalized MWCNTs on the defective lattice sites.[34] Apart from this, no such prominent dual peaks were present in Raman spectra of MTX drug. However, in case of MTX, peaks at 1605 cm^{-1}, 1209 cm^{-1}, 1658 cm^{-1} and 772 cm^{-1} corresponds to NH_2 bending vibrations, CH_2 bending, C=O stretching and C–N stretching vibrations respectively.[35] These peaks of the native drug along with D and G band can be clearly observed in MTX-MWCNTs conjugate which implies the successful conjugation of MTX with the surface of MWCNTs.

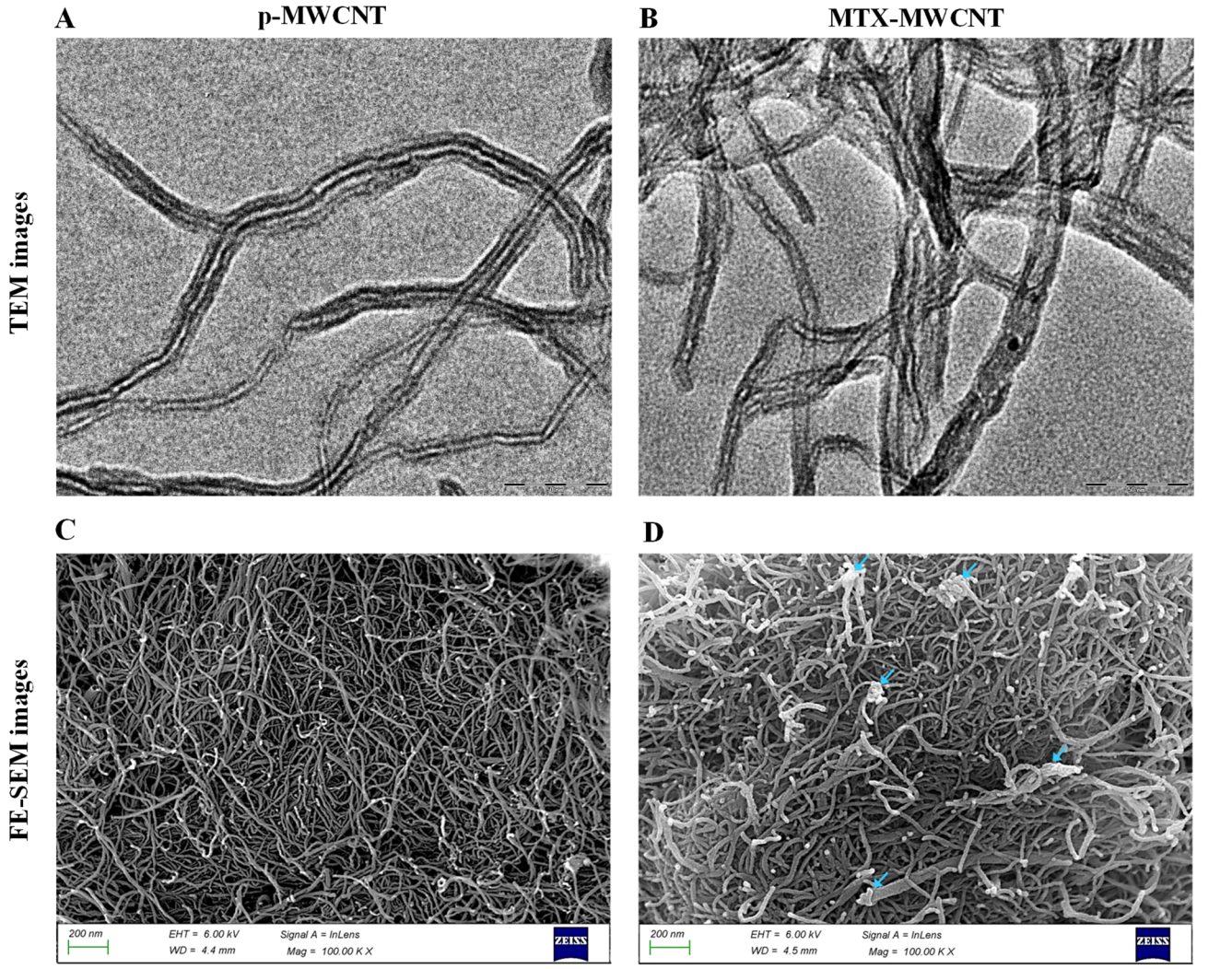

Fig. 2 Electron microscopy-based characterization of p-MWCNTs and MTX-MWCNTs. (A) TEM images displaying the characteristic tubular hollow structure of p-MWCNTs. (B) TEM images of MTX-MWCNT nanoconjugate showing rougher surface with increased diameter. (C) FE-SEM images of p-MWCNTs revealing tubular and entangled structure of MWCNTs. (D) FE-SEM images of MTX-MWCNTs showing the presence of bundled clusters and thickened walls as a result of surface modification and drug conjugation. Scale bar – TEM = 50 nm; FE-SEM = 200 nm.

3.4 X-ray photoelectron spectroscopy (XPS) analysis

X-ray Photoelectron Spectroscopy (XPS) was further done for the evaluation of elemental structure confirm the conjugation of MTX with MWCNTs by analysing the presence of nitrogen peak in MTX-MWCNT conjugate (Fig. 1C). Sharp peaks at binding energies of 284.08 eV and 532.08 eV corresponded to carbon 1 s and oxygen 1s respectively in p-MWCNTs which is associated to its graphitic structure.[15] The carbon peak is consistent with sp^2 C–C bonds with graphitic carbon.[36] In case of MTX, prominent peaks at binding energies 285.08, 399.08 and 532.08 corresponded to carbon 1s, nitrogen 1s and oxygen 1s respectively.[37] The 1s nitrogen peak arises due to the presence of amine and heterocyclic nitrogen groups present in the MTX molecule.[15] The presence of sharp peak at 399.08 eV corresponding to nitrogen 1s in addition to carbon 1s and oxygen 1s peaks at 284.08 eV and 532.08 eV respectively provides direct evidence of MTX attachment onto MWCNT.

3.5 Transmission electron microscopy (TEM) analysis

Transmission Electron Microscopy (TEM) was used for the analysis of the 2D morphology and the nanometric size of the synthesized nanoconjugate. MWCNTs appeared as long tubular intertwined hollow structures suitable for drug loading.[38] The average diameter of the p-MWCNTs (Fig. 2A) and MTX-MWCNTs (Fig. 2B) was found to be 9.65 ± 1.3 nm and 17.05 ± 2.2 nm respectively which clearly indicated significant increase in the diameter of p-MWCNTs after its conjugation with MTX.[31] Furthermore, the surface of MTX-MWCNTs was observed to be rougher and irregular as compared to the p-MWCNTs due to oxidation and surface modification. The formation of interconnected networks corresponds to the surface functionalization and drug conjugation (Fig. S2).[39] However, no significant alteration was observed in the structural integrity of MWCNT even after rigorous oxidation followed by MTX conjugation.[40]

3.6 Field emission scanning electron microscopy (FE-SEM) analysis

Field Emission Scanning Electron Microscopy (FE-SEM) revealed high resolution 3D morphology and surface topology of p-MWCNTs (Fig. 2C) and MTX-MWCNTs (Fig. 2D). The long, tubular and loosely entangled network of cross connected MWCNTs can be clearly evidenced by FE-SEM. In contrast, MTX-MWCNTs exhibited pronounced surface roughening, and the presence of bundled clusters along the tube walls. These morphological changes coincide with the localized thickening of tube walls in MTX-MWCNTs and such structural distortion is expected after covalent conjugation of MTX with MWCNTs.[41] The average diameters of p-MWCNTs and MTX-MWCNTs were found to be 12.05 ± 1.0 nm and 25.93 ± 2.0 nm, respectively. This increase in diameter significantly aligned with the TEM findings and size analysis. The conjugation of MTX with MWCNTs has not significantly altered the native tubular structure, however minor differences can be observed after the non-uniform conjugation of MTX with MWCNTs which may be due to the targeted drug conjugation at particular functional groups.[42]

Table 1 Tabular representation of zeta potential (mV), PDI, and particle size (nm) of p-MWCNTs and MTX-MWCNTs. The table summarizes the surface charge (zeta potential), PDI and average hydrodynamic diameter of p-MWCNTs and MTX-MWCNTs as determined by dynamic light scattering (DLS) analysis. Values are expressed as mean ± SEM of three independent measurements

Compounds	Zeta potential (mV)	PDI	Particle size (nm)
p-MWCNT	−21.915 ± 0.8	0.7 ± 0.14	126.5 ± 11
MTX-MWCNT	−32.73 ± 0.4	0.3 ± 0.07	231.5 ± 20

3.7 Zeta potential and DLS analysis

Zeta potential and DLS analysis was carried out for the analysis of the stability and dispersibility of the MWCNTs in colloidal dispersion. The zeta potential, polydispersity index (PDI) values and particle size of p-MWCNTs and MTX-MWCNTs has been mentioned in Table 1. The lower magnitude of zeta potential of p-MWCNTs indicates weak electrostatic repulsion between the particles and higher tendency to form agglomerates.[23] On the other hand, the zeta potential of MTX-MWCNTs became more negative because of the engagement of the free amine groups in the formation of amide bond which reduces the availability of positively charged amine groups resulting in an increased overall negative charge.[43,44] Moreover, the increase in the magnitude of the zeta potential of MTX-MWCNTs pertains to stronger electrostatic repulsion between the particles with significant electrical stability thereby preventing the formation of agglomerates.[43] The observed increase in particle size after conjugation align significantly with the TEM and FE-SEM findings that revealed increased diameter and this can be attributed to the successful addition of MTX molecules onto the surface of p-MWCNTs.[15] Apart from this, the PDI of MTX-MWCNTs was found to be lower as compared to the native drug which signifies that the drug nanoconjugates have better particle size distribution, enhanced solubility and improved homogenous dispersion.[16]

3.8 MTX-MWCNTs demonstrated potent cytotoxicity in cancer cells with minimal effects on normal cells

The synthesized nanoconjugate displayed significant cytotoxic activity against MCF-7, MDA-MB 231 and HeLa cells (Fig. 3). The cytotoxic potential of MTX-MWCNTs increased with increasing dose resulting in reduced cell viability in a dose-dependent manner. The IC_{50} value which is the minimum concentration of MTX-MWCNTs required to inhibit 50% cell viability was found to be 28.04 ± 1.3, 20.4 ± 1.6 and 21.8 ± 1.3 μg mL^{-1} for MCF-7, MDA-MB 231 and HeLa cancer cells respectively. On the other hand, the IC_{50} value of the positive control MTX was found to be 34.4 ± 1.1, 24.5 ± 2.7 and 25.7 ± 0.4 μg mL^{-1} against MCF-7, MDA-MB 231 and HeLa cancer cells respectively. Apart from this, the IC_{50} values of MTX-MWCNTs and MTX against HEK 293T cells was found to be 193.81 ± 3.2 and 84.3 ± 5.3 μg mL^{-1} respectively[45] (Fig. S3). The IC_{50} values of MTX-MWCNTs in non-cancerous cells was found to be higher than

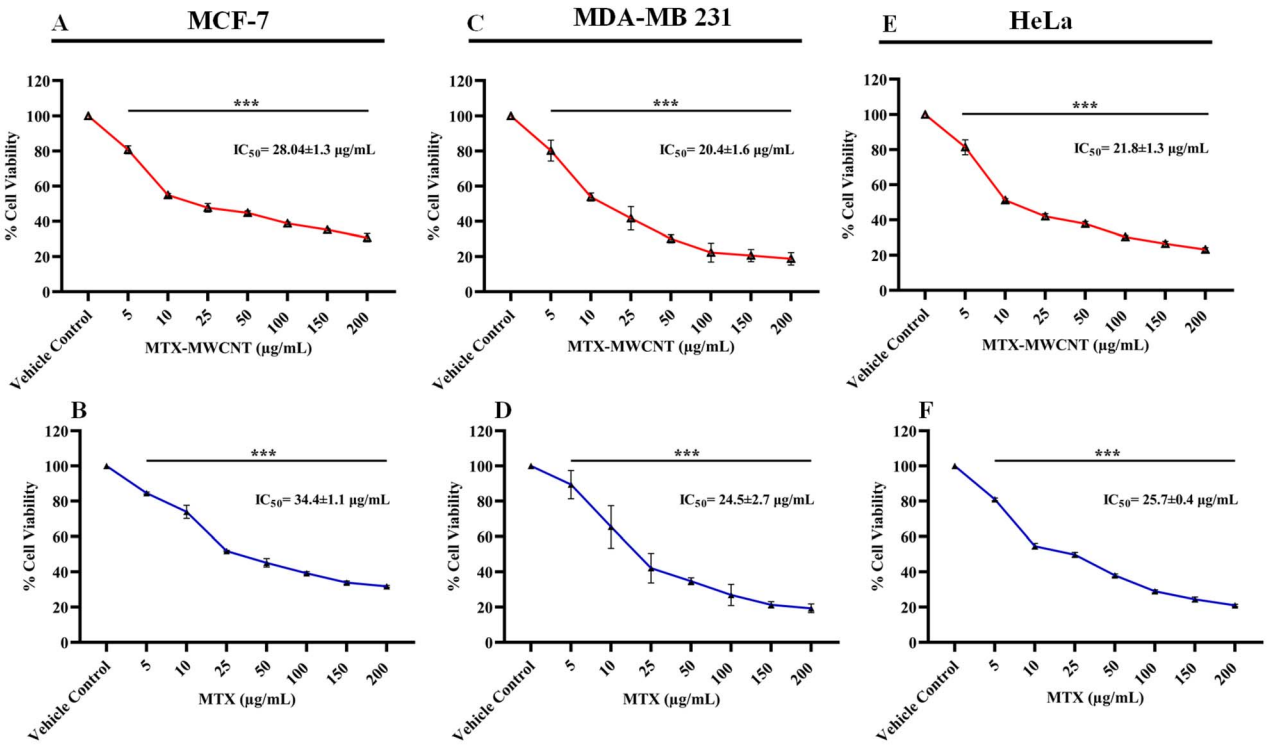

Fig. 3 Representation of cytotoxic potential of MTX-MWCNTs and MTX through MTT assay. The experiment was performed against (A and B) MCF-7 (C and D) MDA-MB 231 and (E and F) HeLa cancer cells performed in triplicates and the data is presented as mean ± SEM of % cell viability. Statistical analysis was carried out using one-way ANOVA followed by Dunnett's multiple comparison test by comparing mean of each treated group to vehicle control. Statistical significance is indicated as follows: *$p < 0.05$, **$p < 0.01$ and ***$p < 0.001$.

that of cancerous cells, which suggested significant anti-proliferative potential of MTX-MWCNTs against cancer cells and biocompatibility toward normal cells.[19] In past investigations, several studies have focused on targeting breast cancer by loading therapeutic agents onto CNTs. For instance, in a recent research work, the cytotoxicity of mitoxantrone loaded SWCNTs was assessed against MDA-MB 231 breast cancer cells.[46] In a past study, MTX was conjugated to aminated MWCNTs to test its cytotoxicity against MDA-MB 231 cells in which cytotoxic effect was observed at relatively higher dose.[32] However, it has been evidenced that carboxylated MWCNTs are more stable as compared to the aminated ones.[47] Based on this work, our research was focused on the evaluation of cytotoxicity of MTX conjugated to carboxylated MWCNTs against cancer cells and the IC_{50} was attained at lower dose. In addition to this, MTX has been co-delivered by being loaded onto several other nano-platforms including mesoporous NPs,[48] dendrimers,[49] magnetic NPs,[50] pullulan NPs[51] and QDs[52] for targeting HeLa cancer cells. Therefore, in addition to breast cancer cells, the cytotoxicity of MTX-MWCNTs were also evaluated against HeLa cells that displayed significant results supporting their further investigation in subsequent *in vitro* studies.

3.9 MTX-MWCNTs exhibited minimal hemolytic activity indicating significant hemocompatibility

Hemolysis assay is an *in vitro* experiment conducted to assess the extent of damage to the RBC membrane caused in response to increasing concentrations of MTX-MWCNTs for evaluating its hemocompatibility. Several chemotherapeutic drugs have been reported to trigger the rupture of RBCs resulting in hemolytic anaemia which is considered as a major toxicity related side effect.[53] Therefore, the safety profile of MTX-MWCNTs was evaluated against human RBCs to assess its hemocompatibility. As shown in Fig. 4A, MTX-MWCNTs displayed negligible hemolytic effects up to a concentration of 100 μg mL^{-1}, with no observable significant hemolysis under these conditions. From the graphical representation as shown in Fig. 4B, it can be observed that the % hemolysis remained below 50% even at the highest tested concentration of 1000 μg mL^{-1}, indicating a dose-dependent response but relatively low overall hemolytic potential. Microscopic examination of RBC morphology further supported these findings (Fig. 4C). No signs of RBC rupture were observed at concentrations below 100 μg mL^{-1}.[54] However, at concentrations ≥100 μg mL^{-1}, a gradual increase in damaged RBCs was evident correlating with increasing dose. These results suggest that MTX-MWCNTs are hemocompatible at lower concentrations, with mild to moderate hemolytic effects at higher doses.

3.10 MTX-MWCNTs inhibited blood vessel formation in CAM assay displaying significant anti-angiogenic potential

The anti-angiogenic effect of MTX-MWCNTs at different concentrations was evidenced through *ex vivo* CAM assay as depicted in Fig. 5. After 48 hours of incubation, the vehicle

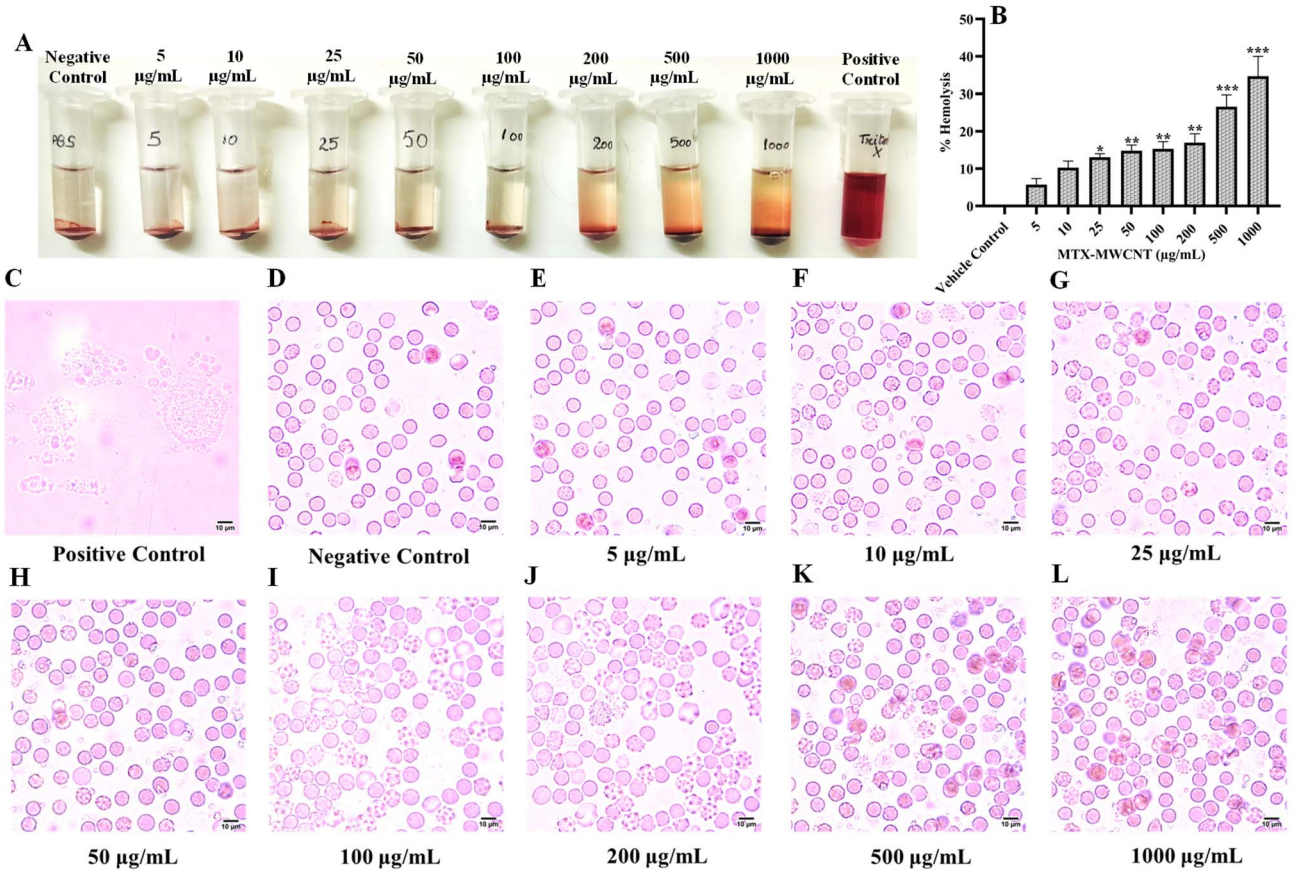

Fig. 4 *In vitro* hemolysis assay of MTX-MWCNTs for the evaluation of hemocompatibility. (A) Visual representation of increasing hemolytic effect of MTX-MWCNTs on RBCs in a dose-dependent manner. (B) Graphical representation of % hemolysis with increasing concentration of MTX-MWCNTs revealing less than 50% hemolysis even at the highest tested concentration of 1000 µg mL^{-1} and the statistical significance was analyzed by comparing mean of vehicle control to the mean of each treated groups using one way ANOVA followed by Dunnett's multiple comparison test (*$p < 0.05$, **$p < 0.01$ and ***$p < 0.001$). (C–L) Microscopic illustration of hemolytic effect of MTX-MWCNTs on RBCs depicting minimal damage at concentrations below 100 µg mL^{-1}. Scale bar = 10 µm.

control group (Fig. 5C) demonstrated normal embryonic development and well-organized, branching of blood vessels pertaining to actively vascularized CAM. In contrast, embryos treated with MTX-MWCNTs exhibited dose-dependent inhibition of blood vessel formation. At lower concentrations, a mild decrease in branching of vessels was observed, while at higher concentrations, a marked reduction in blood vessel formation was evident. The quantitative analysis also validated significant reduction in angiogenic parameters in the 10 µg mL^{-1} treated group compared with the control (Table S1). However, at higher concentrations, prominent suppression of angiogenesis was visually observed after 48 hours of incubation due to which software-based quantification of vascular parameters was not feasible for further treated groups. Angiogenesis is a critical hallmark of cancer progression, as rapid tumor progression requires sustained vascular support for oxygen and nutrient supply. Therefore, inhibition of neovascularization is considered as a powerful therapeutic strategy in oncology. Recent studies have demonstrated that nanoformulations can significantly enhance the anti-angiogenic potential of traditional chemotherapeutics. For instance, polymeric nano-encapsulated systems combining metal oxide NPs with doxorubicin have demonstrated synergistic inhibition of tumor vascularization in both CAM and *in vivo* melanoma models, with improved therapeutic outcomes compared to native drug alone.[55] Similarly, folic acid-targeted liposomal nanoformulations have also displayed enhanced tumor specificity and stronger anti-angiogenic effects in CAM assays, highlighting the importance of nano-enabled targeting and controlled drug delivery in disrupting tumor vasculature.[56] The anti-angiogenic properties of MWCNTs have also been reported previously, not only in *ex vivo* CAM assays but also in *in vivo* models, where they were shown to inhibit neovascularization.[57] Therefore, the performed CAM assay suggests that MTX-MWCNTs interfere with the angiogenic processes required for cell proliferation.

3.11 MTX-MWCNTs demonstrated significant antiproliferative potential in cancer cells

Cancer cells are significantly characterized by rapid cell proliferation resulting in the formation of malignant tumor in some cases. The degree of proliferation of the adherent cells was evaluated by using crystal dye stain. Crystal dye is a basic dye that binds with the negatively charged protein and DNA of live and adhered cells. The cell viability is reduced upon treatment with

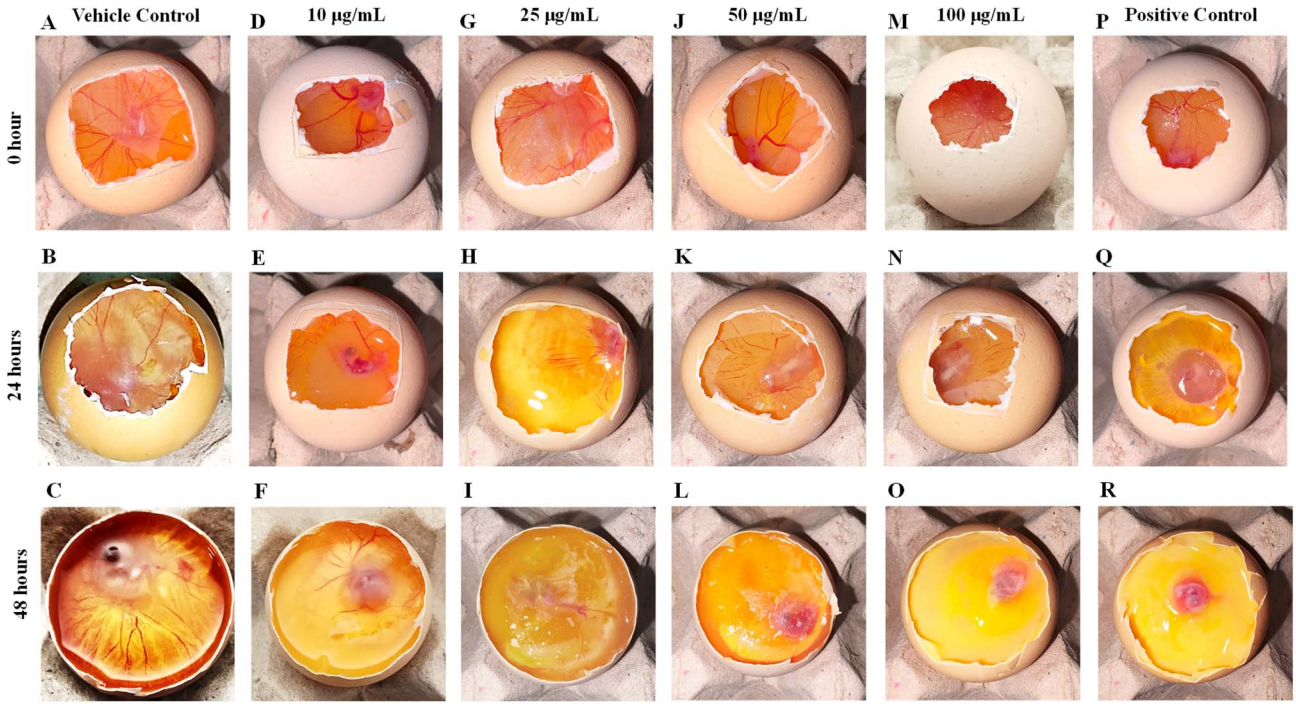

Fig. 5 *Ex vivo* CAM assay showing the effect of MTX-MWCNTs on angiogenesis at different concentrations. Representative CAM images after treatment with (A–C) vehicle control; (D–F) MTX-MWCNTs at 10 μg mL^{-1}; (G–I) MTX-MWCNTs at 25 μg mL^{-1}; (J–L) MTX-MWCNTs at 50 μg mL^{-1}; (M–O) MTX-MWCNTs at 100 μg mL^{-1} and (P–R) positive control at 0 hours, 24 hours, and 48 hours respectively. The images represent distinct vascular responses, where the control groups have demonstrated well-developed progressive vasculature over time, whereas MTX-MWCNTs treated groups have displayed significant reduction in vessel branching with increasing incubation time in a dose and time-dependent manner.

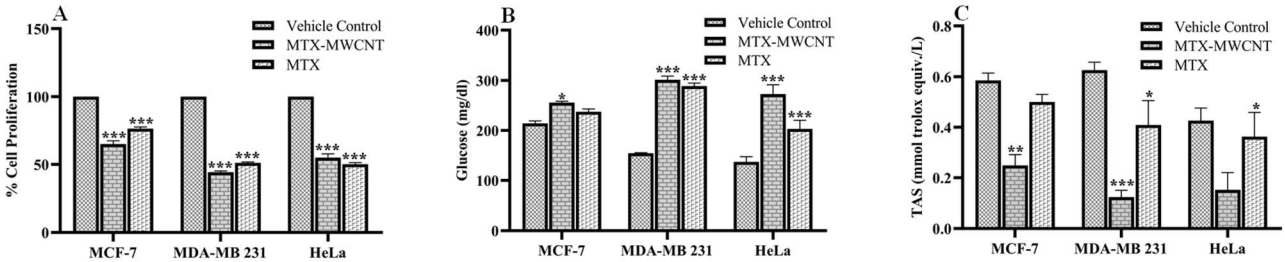

Fig. 6 Evaluation of cytotoxic potential of MTX-MWCNTs against MCF-7, MDA-MB 231 and HeLa cells through biochemical assays. (A) Reduced % cell proliferation demonstrated significant anti-proliferative potential of MTX-MWCNTs. (B) The elevated concentration of residual glucose in the medium after treatment indicated decreased glucose uptake due to cell death. (C) Decreased TAS (mmol Trolox equiv. per L) after treatment revealed the induction of significant oxidative stress responsible for increased cell death. Representative data of three independent experiments are expressed as mean ± SEM and two-way ANOVA followed by Dunnett's multiple comparison test was applied to determine the statistical significance by comparing the mean of vehicle control to the mean of treated groups (*$p < 0.05$, **$p < 0.01$ and ***$p < 0.001$).

MTX-MWCNTs which was examined by determining and comparing the percentage of stained control and treated cells. The dead and non-viable cells exhibit reduced colour intensity as compared to the viable ones, which aids in the determination of the cell proliferation rate. Upon treatment with MTX-MWCNTs at IC_{50} concentration, all three cancer cells displayed reduced % cell proliferation rate as compared to the control ones which significantly aligned with the results obtained from cell viability assay (Fig. 6A). The percentage cell proliferation of MTX-MWCNTs treated MCF-7, MDA-MB 231 and HeLa cells was found to be 65.1 ± 2.38, 44.36 ± 0.81 and 55.03 ± 2.78 respectively whereas in case of MTX treated MCF-7, MDA-MB 231 and HeLa cells, % cell proliferation was found to be 76.4 ± 1.33, 51.1 ± 0.69 and 50.2 ± 1.12 respectively. One of the previous findings have also used crystal violet assay to assess the cytotoxic potential of zinc ferrite NPs against breast cancer cells.[58] In another work, the cytotoxic potential of cisplatin loaded ZnO NPs was evaluated against SiHa cervical squamous cancer cells.[59] Recently, crystal violet assay has also been used to test the anticancer activity of pirfenidone which is an FDA-approved drug against TNBC cells.[60] Therefore, the

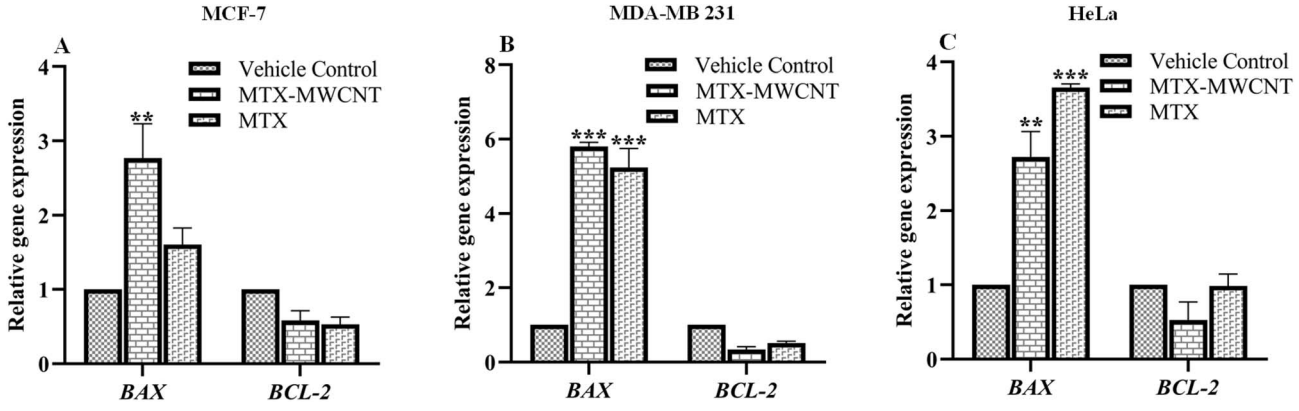

Fig. 7 qRT-PCR data displaying differential expression of pro-apoptotic (*BAX*) and anti-apoptotic (*BCL-2*) genes. Representative graphs demonstrate the upregulation of *BAX* and downregulation of *BCL-2* gene with respect to vehicle control after treatment with MTX-MWCNTs and MTX at IC_{50} concentration against (A) MCF-7, (B) MDA-MB 231, and (C) HeLa cancer cells. Representative data of two independent experiments are expressed as mean ± SEM and two-way ANOVA followed by Tukey's multiple comparison test was used to determine the statistical significance by comparing mean of the vehicle control to the mean of treated groups (*$p < 0.05$, **$p < 0.01$ and ***$p < 0.001$).

obtained results clearly demonstrate that MTX-MWCNTs treated cancer cells displayed lesser cell proliferation rate as compared to native MTX.

3.12 MTX-MWCNTs indicated significant metabolic alteration through reduced glucose uptake

After the evaluation of the hemocompatibility profile and anti-angiogenic activity, the biochemical alteration in cancer cells post treatment with MTX-MWCNTs at IC_{50} concentration was assessed. Cancer cells rely on aerobic glycolysis to meet their high demand of glucose for rapid proliferation. Glucose estimation was performed to explore whether the synthesized nanoconjugate could influence cellular metabolism post treatment with MTX-MWCNTs at IC_{50} concentration. The glucose concentration in the culture media of treated cells was compared with that of control cells, revealing a higher level of unconsumed glucose content in the treated cells due to altered glucose metabolism (Fig. 6B). The glucose content in the culture media of MCF-7, MDA-MB 231 and HeLa control cells was found to be 204.54 ± 4.9, 154.36 ± 1.05 and 137.29 ± 10.04 mg dl^{-1} respectively. However, after treatment with MTX-MWCNTs, the increased glucose content was found to be 255.92 ± 2.45, 301.54 ± 7.2 and 272.92 ± 18.5 mg dl^{-1} for MCF-7, MDA-MB 231 and HeLa cells respectively. In case of treatment with positive control MTX, the glucose content was slightly lower than MTX-MWCNTs treated cells and was found to be 237.4 ± 5.65, 288.81 ± 6.11 and 203 ± 17.36 mg dl^{-1} for MCF-7, MDA-MB 231 and HeLa cells respectively. According to one of the past findings, reduced glucose metabolism of CT26 cancer cells when treated with resveratrol-loaded polymeric NPs under *in vitro* conditions was correlated with suppressed tumor proliferation.[61] Furthermore, fungal-mediated green-based AgNPs have also resulted in suppressed glucose metabolism in breast cancer cells in one of the recent findings.[62] Hence, the aforementioned results suggest that the synthesized nanoconjugates were capable of altering glucose metabolism which correlated with reduced glucose uptake and decreased cancer cell viability.

3.13 MTX-MWCNTs demonstrated reduced TAS due to oxidative stress-mediated cell death

Cancer cells inherently maintain higher basal ROS levels than normal cells due to accelerated metabolism, mitochondrial dysfunction, and oncogene-driven signaling. To prevent ROS from reaching cytotoxic levels, they rely heavily on NADPH-dependent glutathione (GSH) and other enzymatic antioxidants to neutralize ROS and maintain redox homeostasis. The TAS of the vehicle control treated cells was found to be significantly higher compared to the treated groups (Fig. 6C). After treatment, a marked decrease in TAS was observed in both MTX-MWCNT and MTX treated groups, with the reduction being more prominent in MTX-MWCNT treated cells. This suggests that the MWCNT mediated delivery of MTX may have enhanced the cellular uptake resulting in elevated oxidative stress. From a research *in vivo*, it has been evidenced that MWCNTs are capable of inducing oxidative stress resulting in decreased total antioxidant status and increased oxidative stress markers.[63] The observed decline in TAS in MTX-MWCNT and MTX treated cancer cells indicates a disruption of the cellular redox balance and antioxidant defense system with subsequent induction of oxidative stress.

3.14 MTX-MWCNT nanoconjugates modulated pro-apoptotic *BAX* and anti-apoptotic *BCL-2* gene expression to promote apoptosis

The expression levels of apoptosis-related genes *BAX* and *BCL-2* were analyzed in MCF-7, MDA-MB 231, and HeLa cells after treatment with MTX-MWCNTs and MTX by real-time amplification using qRT-PCR (Fig. 7). The vehicle control was set as the reference group with a fold change of 1 for both genes. In MCF-7 cancer cells, *BAX* gene expression was upregulated with a fold change of 2.76 ± 0.46 (*p*-value 0.004) and 1.6 ± 0.22 (*p*-value 0.275) while relative expression of *BCL-2* gene was downregulated with a fold change of 0.45 ± 0.13 (*p*-value 0.543) and 0.52 ± 0.09 (*p*-value 0.451) in MTX-MWCNT and MTX treated cells respectively. Likewise, in MDA-MB

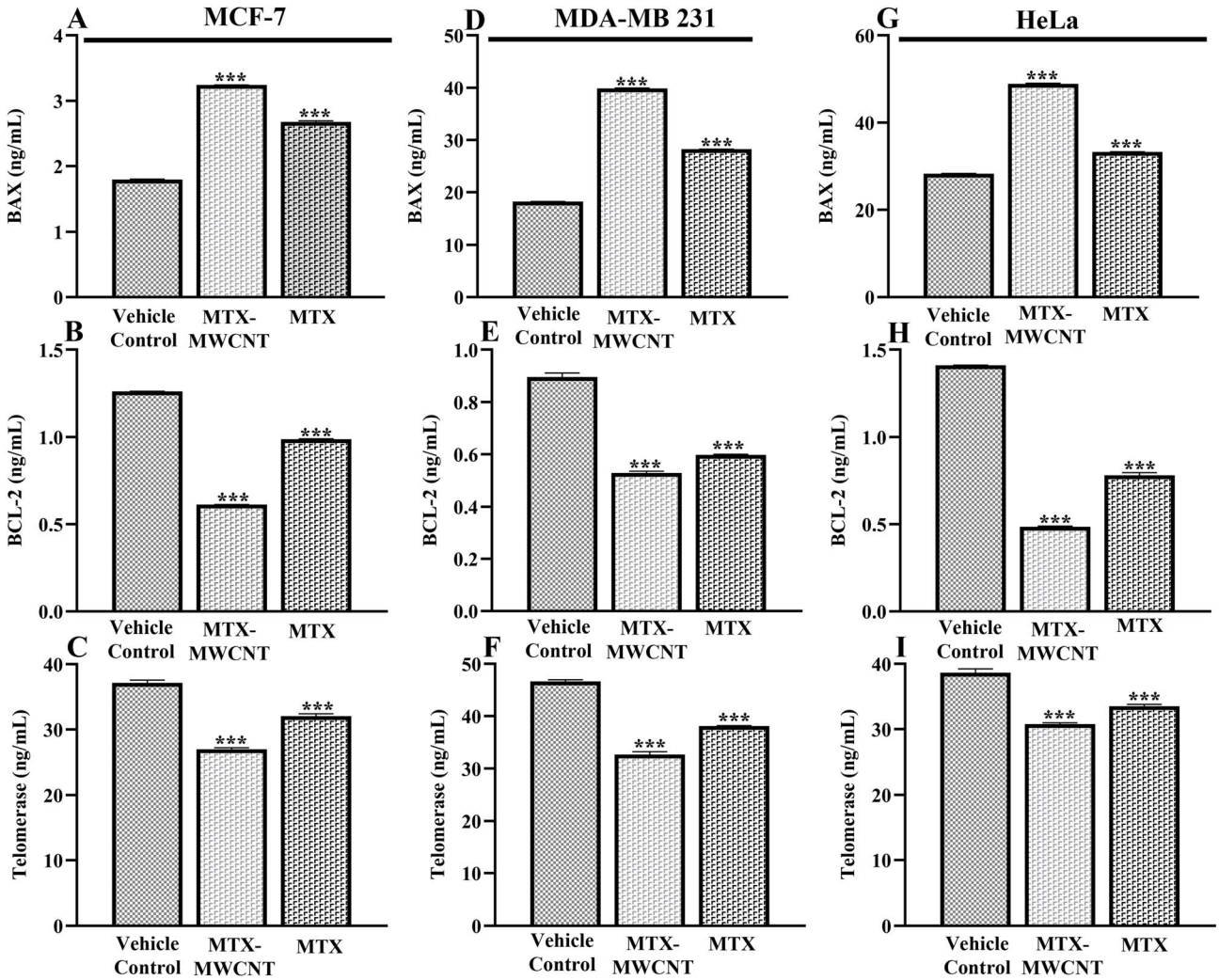

Fig. 8 Quantitative analysis of BAX, BCL-2, and telomerase protein levels determined by kit-based sandwich ELISA. Representative graphs correspond to the relative expression levels of BAX, BCL-2 and telomerase after treatment with MTX-MWCNTs in (A–C) MCF-7, (D–F) MDA-MB 231, and (G–I) HeLa cancer cells respectively. Data are expressed as mean ± SEM of three independent experiments and statistical significance was determined by comparing mean of vehicle control to the mean of treated groups using one-way ANOVA followed by Dunnett's multiple comparison test (*$p < 0.05$, **$p < 0.01$ and ***$p < 0.001$).

231 cancer cells, the expression of *BAX* gene was upregulated with a fold change of 5.8 ± 0.11 (*p*-value 0.000) and 5.23 ± 0.51 (*p*-value 0.000) while the expression of *BCL-2* gene was downregulated with a fold change of 0.34 ± 0.07 (*p*-value 0.166) and 0.51 ± 0.04 (*p*-value 0.335) in MTX-MWCNT and MTX treated cells respectively. Similarly, in HeLa cancer cells, *BAX* gene expression was upregulated with a fold change of 2.72 ± 0.34 (*p* value 0.001) and 3.65 ± 0.05(*p*-value 0.000) whereas *BCL-2* gene was downregulated with a fold

Table 2 Tabular representation of quantitative analysis of BAX, BCL-2 and telomerase protein levels after treatment with MTX-MWCNT compared with MTX treated and vehicle control groups in MCF-7, MDA-MB 231 and HeLa cancer cells. Data are presented as mean ± SEM of experiment performed in triplicates

Compounds	BAX (ng mL^{-1})	BCL-2 (ng mL^{-1})	Telomerase (ng mL^{-1})
Vehicle control	MCF-7 – 1.79 ± 0.007	MCF-7 – 1.26 ± 0.0008	MCF-7 – 37.15 ± 0.415
	MDA-MB 231 – 18.21 ± 0.029	MDA-MB 231 – 0.89 ± 0.016	MDA-MB 231 – 46.65 ± 0.324
	HeLa – 28.28 ± 0.037	HeLa – 1.41 ± 0.001	HeLa – 38.65 ± 0.343
MTX-MWCNT	MCF-7 – 3.24 ± 0.001	MCF-7 – 0.61 ± 0.0005	MCF-7 – 26.99 ± 0.214
	MDA-MB 231 – 39.88 ± 0.074	MDA-MB 231 – 0.52 ± 0.006	MDA-MB 231 – 32.7 ± 0.521
	HeLa – 48.92 ± 0.141	HeLa – 0.48 ± 0.004	HeLa – 30.78 ± 0.114
MTX	MCF-7 – 2.67 ± 0.014	MCF-7 – 0.98 ± 0.002	MCF-7 – 32.05 ± 0.371
	MDA-MB 231 – 28.25 ± 0.014	MDA-MB 231 – 0.59 ± 0.002	MDA-MB 231 – 38.08 ± 0.081
	HeLa – 33.25 ± 0.079	HeLa – 0.78 ± 0.015	HeLa – 33.52 ± 0.172

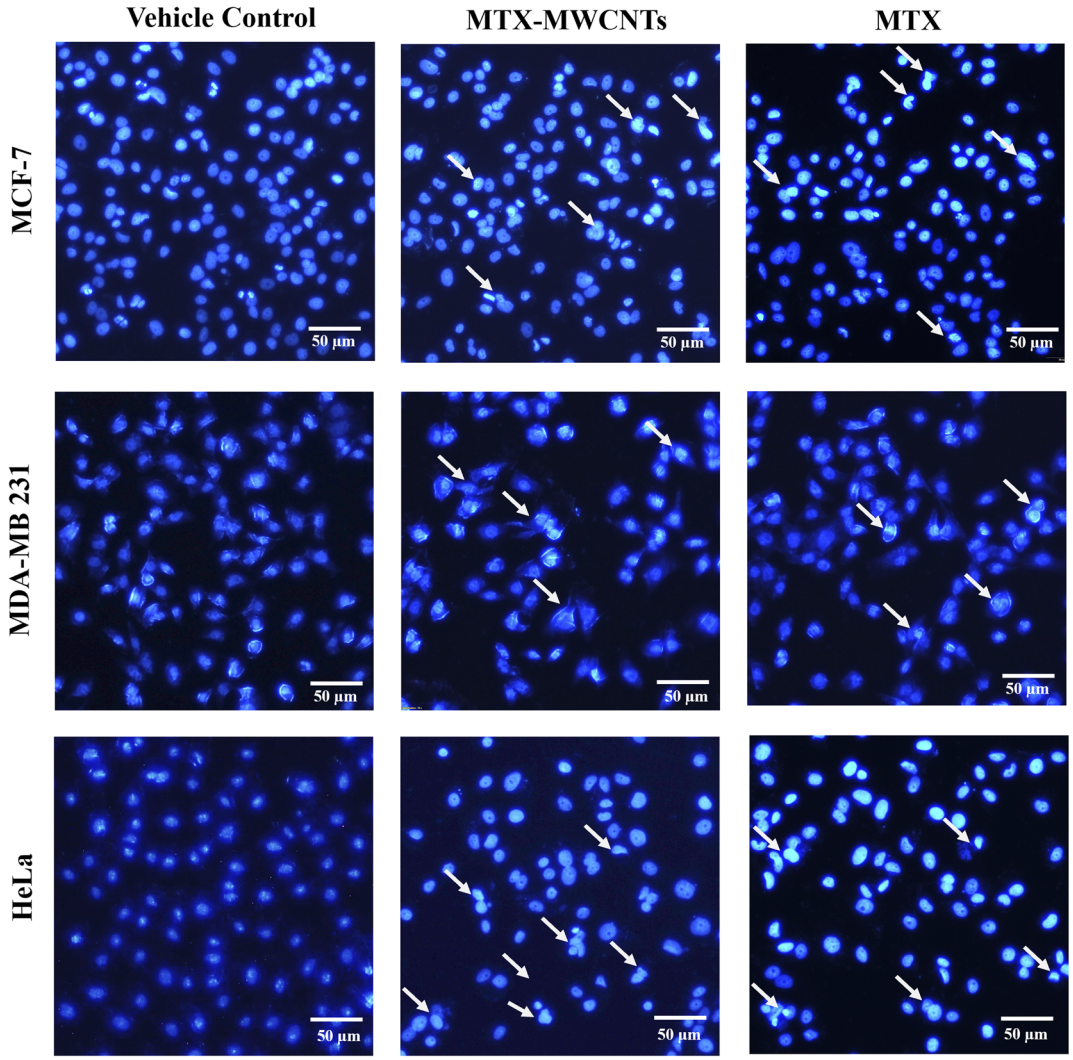

Fig. 9 Evaluation of alteration in nuclear morphology using DAPI staining at IC_{50} concentration. Representative DAPI images of (A–C) vehicle control; (D–F) MTX-MWCNTs-treated group and (G–I) MTX-treated group of MCF-7, MDA-MB 231 and HeLa cancer cells. The images displayed significant alteration in nuclear morphology in the treated groups as compared to the vehicle control groups in all three cancer cells. Scale bar = 50 µm.

change of 0.52 ± 0.24 (p-value 0.243) and 0.9 ± 0.16 (p-value 0.998) in MTX-MWCNT and MTX treated cells respectively. The presented results significantly indicate that MTX-MWCNTs treatment strongly induce pro-apoptotic signaling in cancer cells by altering *BAX* and *BCL-2* gene expression levels.[64]

3.15 MTX-MWCNTs demonstrated significant alteration in BAX, BCL-2 and telomerase protein levels

The quantification of expression level of BAX, BCL-2 and telomerase proteins after treatment was done by kit-based sandwich ELISA in MCF-7, MDA-MB-231, and HeLa cells for further validation of qRT-PCR findings. The results revealed a significant upregulation of BAX protein, indicating enhanced pro-apoptotic activity, whereas a marked downregulation of BCL-2 and telomerase proteins was observed across all three cell lines compared to the vehicle control (Fig. 8). BAX, BCL-2 and telomerase protein concentration of vehicle control, MTX-MWCNT and MTX treated cells in MCF-7, MDA-MB 231and HeLa cancer cells have been presented in tabular form in Table 2. In a past study, it has been demonstrated that valproic acid-treated MCF-7 cells exhibited reduced telomerase activity which resulted in significant upregulation of the pro-apoptotic protein BAX and downregulation of the anti-apoptotic protein BCL-2, suggesting a mechanistic link between telomerase suppression and enhanced apoptotic signaling.[65] Our findings also correlate with the qRT-PCR results, confirming that MTX-MWCNT nanoconjugates effectively induce apoptosis and inhibit tumor proliferation at the protein level.

3.16 MTX-MWCNTs induce significant alteration in nuclear morphology

The evaluation of alteration in nuclear morphology was then performed through DAPI staining for the assessment of apoptosis induced by MTX-MWCNT treatment (Fig. 9). DAPI is a widely used fluorescent dye that selectively binds to the adenine-thymine rich regions of double stranded DNA. After

binding to DNA, DAPI exhibits strong blue fluorescent signal upon excitation, allowing for clear visualization of the nuclear structure under fluorescence microscope. The vehicle control group (Fig. (9A–C)) displayed uniformly stained nuclei with intact morphology, indicating normal cellular architecture. In contrast, cells treated with MTX-MWCNT (Fig. 9D–F) and MTX (Fig. 9(G–I)) at their respective IC_{50} concentrations exhibited significant nuclear alterations characteristic of apoptosis. Specifically, treated cells displayed nuclear shrinkage, chromatin condensation and greater number of irregular nuclei and apoptotic bodies. The observed nuclear morphological changes significantly align with the cytotoxicity results and indicate significant apoptotic potential of the synthesized nanoconjugate.

4. Conclusion

In the present research work, MTX-MWCNT nanoconjugate was successfully developed as a potential anticancer delivery system with enhanced efficacy and biocompatibility. r-MWCNTs were first purified and then p-MWCNTs were carboxylated to introduce carboxyl groups, enabling efficient covalent conjugation of MTX through amide bond formation. This modification not only facilitated drug conjugation but also enhanced aqueous dispersibility and colloidal stability of the MWCNTs, as confirmed by dispersion solubility test. Following synthesis, comprehensive physicochemical characterization of the nanoconjugate was done using FTIR, Raman spectroscopy, XPS, TEM, FE-SEM, and DLS which validated the successful conjugation of MTX onto the functionalized nanotube surface. The spectral shifts in FTIR and Raman spectra, along with characteristic binding energy changes in XPS profiles, confirmed the presence of characteristic functional groups and the formation of amide bond. On the other hand, microscopic evaluation through TEM and FE-SEM revealed significant increase in roughness and localized thickening after conjugation. The DLS data further supported improved dispersion and reduced aggregation, indicative of enhanced surface modification.

The biological evaluations of MTX-MWCNT nanoconjugate exhibited significant cytotoxic and anti-angiogenic potential. The cell viability assay revealed effective cytotoxicity of MTX-MWCNT against the tested cancer cells and significant biosafety toward normal cells. *In vitro* hemolysis assay further confirmed the hemocompatibility of MTX-MWCNT and anti-angiogenic potential assessed through CAM assay revealed a dose-dependent inhibition of neovascularization in MTX-MWCNT treated chick embryos. The cytotoxicity-induced metabolic alteration was further validated through biochemical assays. Glucose uptake and cell proliferation assays corresponded to the decreased metabolic activity and viability of the treated cells as compared to the vehicle control. Likewise, significant reduction in TAS was observed in MTX-MWCNT treated cells compared to vehicle control, indicating oxidative stress-mediated cell death responsible for apoptosis. Furthermore, molecular analysis through qRT-PCR showed a distinct upregulation of the pro-apoptotic *BAX* gene and downregulation of the anti-apoptotic *BCL-2* gene which also validated the activation of apoptosis. These findings were further supported by ELISA-based protein quantification, where increased *BAX* and decreased *BCL-2* protein levels, along with downregulation of telomerase expression, confirmed the promotion of apoptosis. Lastly, DAPI staining was performed to further validate the apoptotic potential of the synthesized nanoconjugate. The alteration in nuclear morphology in the treated groups significantly indicated a shift towards apoptosis through chromatin condensation and nuclear fragmentation. Conclusively, the results demonstrated that covalent conjugation of MTX to functionalized MWCNTs effectively enhances its therapeutic potential by improving stability and apoptotic efficacy while maintaining significant biocompatibility. The MTX-MWCNT nanoconjugate not only addresses the limitations such as poor bioavailability and solubility, but also provides a promising nanoplatform for targeted cancer therapy. Future studies involving *in vivo* pharmacokinetic will further establish its translational potential as an efficient nanotube-based chemotherapeutic system.

Ethical statement

The *in vitro* hemolysis experiment has been approved by Institutional Ethics Committee, Institute of Medical Sciences, Banaras Hindu University, Varanasi under the approval letter number IMS/IEC/2025/7913. The CAM assay was performed using fertilized chicken eggs obtained from a commercial poultry source. Our study involving all CAM experiments were in compliance with relevant institutional guidelines. All animal procedures were performed in accordance with the Guidelines for Care and Use of Laboratory Animals of Banaras Hindu University and approved by the Animal Ethics Committee.

Author contributions

HT: data curation; formal analysis; investigation; methodology; validation; writing-original draft; writing-review & editing; visualization. SS: investigation; methodology; validation; writing-review & editing. VK: methodology; writing-review & editing. ST: data curation; writing-review & editing. AKS: data curation. ASP: data curation. SKS: review and editing. VG: supervision; conceptualization; methodology; formal analysis; funding acquisition; investigation; project administration; resources; software; writing review and editing.

Conflicts of interest

There is no any potential conflict of interest associated with the present manuscript.

Data availability

All the data produced and/or analyzed in the course of this study are presented within this manuscript and its accompanying supplementary information (SI) file. Supplementary information is available. See DOI: https://doi.org/10.1039/d5ra08838k.

Acknowledgements

The present research has been supported by the Institution of Eminence (IoE) Seed Grant, Bridge Grant, Banaras Hindu University (BHU), and by funding from the Council of Science and Technology, Uttar Pradesh to Dr Vibhav Gautam (VG). VG also acknowledges funding support for his laboratory from the ANRF (IRG Scheme; ANRF/IRG/2025/000135/LS), New Delhi, and the Council of Science and Technology, Uttar Pradesh, India. Harshita Tiwari is thankful to Department of Biotechnology (DBT), New Delhi, India, for the award of Junior Research Fellowship (JRF). Swati Singh acknowledges UGC, New Delhi, for the award of Senior Research Fellowship (SRF). Vandana Kumari is grateful to UGC, New Delhi, for the award of Junior Research Fellowship (JRF). The authors express their sincere gratitude to the Director, Institute of Medical Sciences (IMS), BHU, for financial support to the laboratory. The corresponding author, on behalf of all the authors, acknowledges the Central Discovery Centre, BHU, Department of Physics, BHU, Department of Physics, IIT-BHU, and Central Instrumental Facility (CIF), IIT-BHU for providing instrumentation facilities.

References

1 C. K. Thakur, C. Karthikeyan, C. R. Ashby Jr, *et al.*, Ligand-conjugated multiwalled carbon nanotubes for cancer targeted drug delivery, *Front. Pharmacol*, 2024, **15**, 1417399.
2 H. Tiwari, S. Singh, R. Kumar, *et al.*, Novel advancements in nanomaterials-based contrast agents across multimodal imaging and theranostic applications, *Nanoscale Adv.*, 2025, **7**(21), 6753–6773.
3 H. Tiwari, N. Rai, S. Singh, *et al.*, Recent advances in nanomaterials-based targeted drug delivery for preclinical cancer diagnosis and therapeutics, *Bioengineering*, 2023, **10**(7), 760.
4 J. Wang, J. Zhang, M. Xiao, *et al.*, Molecular mechanisms of doxorubicin-induced cardiotoxicity: novel roles of sirtuin 1-mediated signaling pathways, *Cell. Mol. Life Sci.*, 2021, **78**(7), 3105–3125.
5 M. M. Alqahtani, Cisplatin-Induced Renal Failure Measured by Glomerular Filtration Rate (GFR) with 99mTc-DTPA Scans in Cancer Patients: A Systematic Review and Meta-Analysis, *Diagnostics*, 2024, **14**(22), 2468.
6 G. F. Ali, E. H. M. Hassanein and W. R. Mohamed, Molecular mechanisms underlying methotrexate-induced intestinal injury and protective strategies, *Naunyn-Schmiedeberg's Arch. Pharmacol.*, 2024, **397**(11), 8165–8188.
7 H. Shariatifar, F. Ranjbarian, F. Hajiahmadi and A. Farasat, A comprehensive review on methotrexate containing nanoparticles; an appropriate tool for cancer treatment, *Mol. Biol. Rep.*, 2022, **49**(11), 11049–11060.
8 S. Ouellette, R. Shah, S. Razi, G. Ashforth and C. Wassef, Fatal low-dose methotrexate toxicity: a case report and literature review, *Dermatol. Ther.*, 2022, **35**(12), e15945.
9 D. Ezhilarasan, Hepatotoxic potentials of methotrexate: understanding the possible toxicological molecular mechanisms, *Toxicology*, 2021, **458**, 152840.
10 M. Mukhtar, A.-L. Ezra Manicum, B. M. Shojaei, *et al.*, Nanocarriers for methotrexate delivery/codelivery in the frame of cancer diagnostics and treatment: a review, *Front. Biomater. Sci.*, 2023, **2**, 1200670.
11 S. Nitodas, R. Shah and M. Das, Research Advancements in the Mechanical Performance and Functional Properties of Nanocomposites Reinforced with Surface-Modified Carbon Nanotubes: A Review, *Appl. Sci.*, 2025, **15**(1), 374.
12 M. Nabitabar, M. Shaterian, H. Danafar and M. Enhessari, Multi-wall carbon Nanotube surface-based functional nanoparticles for stimuli-responsive dual pharmaceutical compound delivery, *Sci. Rep.*, 2024, **14**(1), 12073.
13 H. Tiwari, S. Singh, S. Sharma, *et al.*, Deciphering the landscape of triple negative breast cancer from microenvironment dynamics and molecular insights to biomarker analysis and therapeutic modalities, *Med. Res. Rev.*, 2025, **45**(3), 817–841.
14 K. Domagała, M. Borlaf, J. Traber, D. Kata and T. Graule, Purification and functionalisation of multi-walled carbon nanotubes, *Mater. Lett.*, 2019, **253**, 272–275.
15 A. Karimi, M. Erfan, S. A. Mortazavi, F. Ghorbani-Bidkorbeh, F. Kobarfard and F. H. Shirazi, Functionalisation of carbon nanotubes by methotrexate and study of synchronous photothermal effect of carbon nanotube and anticancer drug on cancer cell death, *IET Nanobiotechnol.*, 2019, **13**(1), 52–57.
16 A. Karimi, M. Erfan, S. A. Mortazavi, *et al.*, The photothermal effect of targeted methotrexate-functionalized multi-walled carbon nanotubes on MCF7 cells, *Iran. J. Pharm. Res.*, 2019, **18**(1), 221.
17 Z. Huang, L. Xi, Q. Subhani, W. Yan, W. Guo and Y. Zhu, Covalent functionalization of multi-walled carbon nanotubes with quaternary ammonium groups and its application in ion chromatography, *Carbon*, 2013, **62**, 127–134.
18 B. Lubamba, T. Jensen and R. McClelland, Rapid detection of direct compound toxicity and trailing detection of indirect cell metabolite toxicity in a 96-well fluidic culture device for cell-based screening environments: tactics in six sigma quality control charts, *Appl. Sci.*, 2022, **12**(6), 2786.
19 N. Rai, P. Gupta, A. Verma, *et al.*, Ethyl acetate extract of *Colletotrichum gloeosporioides* promotes cytotoxicity and apoptosis in human breast cancer cells, *ACS Omega*, 2023, **8**(4), 3768–3784.
20 N. R. Kokila, B. Mahesh, K. P. Roopa, *et al.*, *Thunbergia mysorensis* mediated nano silver oxide for enhanced antibacterial, antioxidant, anticancer potential and *in vitro* hemolysis evaluation, *J. Mol. Struct.*, 2022, **1255**, 132455.
21 V. Gautam, A. Singh, S. Yadav, *et al.*, Conserved LBL1-ta-siRNA and miR165/166-RLD1/2 modules regulate root development in maize, *Development*, 2021, **148**(1), dev190033.
22 R. Billimoria and P. Bhatt, Chrysin mitigates therapy-induced senescence in breast cancer *via* cGAS-STING pathway inhibition, *Med. Oncol.*, 2025, **42**(10), 445.
23 B. Tserengombo, H. Jeong, E. Dolgor, A. Delgado and S. Kim, Effects of functionalization in different conditions and ball

milling on the dispersion and thermal and electrical conductivity of MWCNTs in aqueous solution, *Nanomaterials*, 2021, **11**(5), 1323.

24 C. Gao, M. Guo, Y. Liu, *et al.*, Surface modification methods and mechanisms in carbon nanotubes dispersion, *Carbon*, 2023, **212**, 118133.

25 D. Park, H. Ju, T. Oh and J. Kim, A p-type multi-wall carbon nanotube/Te nanorod composite with enhanced thermoelectric performance, *RSC Adv.*, 2018, **8**(16), 8739–8746.

26 S. Mohan, O. S. Oluwafemi, S. P. Songca, *et al.*, Completely green synthesis of silver nanoparticle decorated MWCNT and its antibacterial and catalytic properties, *Pure Appl. Chem.*, 2016, **88**(1–2), 71–81.

27 M. B. Askari, Z. T. Banizi, S. Soltani and M. Seifi, Comparison of optical properties and photocatalytic behavior of TiO_2/MWCNT, CdS/MWCNT and TiO_2/CdS/MWCNT nanocomposites, *Optik*, 2018, **157**, 230–239.

28 A. Zaman, T. U. Rashid, M. A. Khan and M. M. Rahman, Preparation and characterization of multiwall carbon nanotube (MWCNT) reinforced chitosan nanocomposites: effect of gamma radiation, *BioNanoSci.*, 2015, **5**, 31–38.

29 S. Zhang, F. Zhang, Y. Pan, *et al.*, Multiwall-carbon-nanotube/cellulose composite fibers with enhanced mechanical and electrical properties by cellulose grafting, *RSC Adv.*, 2018, **8**(11), 5678–5684.

30 B. Álvarez-González, M. Rozalen, M. Fernández-Perales, M. A. Álvarez and M. Sánchez-Polo, Methotrexate gold nanocarriers: loading and release study: its activity in colon and lung cancer cells, *Molecules*, 2020, **25**(24), 6049.

31 J. Kayat, N. K. Mehra, V. Gajbhiye and N. K. Jain, Drug targeting to arthritic region *via* folic acid appended surface-engineered multi-walled carbon nanotubes, *J. Drug Targeting*, 2016, **24**(4), 318–327.

32 M. Joshi, P. Kumar, R. Kumar, *et al.*, Aminated carbon-based "cargo vehicles" for improved delivery of methotrexate to breast cancer cells, *Mater. Sci. Eng., C*, 2017, **75**, 1376–1388.

33 R. Murugesan, Y. Haldorai, L. Sibi and R. Sureshkumar, Ibrutinib conjugated surface-functionalized multiwalled carbon nanotubes and its biopolymer composites for targeting prostate carcinoma, *J. Mater. Sci.*, 2021, **56**(33), 18684–18696, DOI: 10.1007/s10853-021-06559-w.

34 P. G. Carneiro, D. G. Pereira, B. M. O. da Silva, *et al.*, Multifunctional modified carbon nanotubes as potential anti-tumor drug delivery, *Surf. Interfaces*, 2023, **41**, 103211.

35 S. Ayyappan, N. Sundaraganesan, V. Aroulmoji, E. Murano and S. Sebastian, Molecular structure, vibrational spectra and DFT molecular orbital calculations (TD-DFT and NMR) of the antiproliferative drug Methotrexate, *Spectrochim. Acta, Part A*, 2010, **77**(1), 264–275.

36 D. J. Morgan, Comments on the XPS analysis of carbon materials, *C*, 2021, **7**(3), 51.

37 M. Azizi, H. Valizadeh, M. Shahgolzari, *et al.*, Synthesis of self-targeted carbon dot with ultrahigh quantum yield for detection and therapy of cancer, *ACS Omega*, 2020, **5**(38), 24628–24638.

38 W. Zhu, H. Huang, Y. Dong, C. Han, X. Sui and B. Jian, Multi-walled carbon nanotube-based systems for improving the controlled release of insoluble drug dipyridamole, *Exp. Ther. Med.*, 2019, **17**(6), 4610–4616, DOI: 10.3892/etm.2019.7510.

39 J. M. Tan, S. Bullo, S. Fakurazi and M. Z. Hussein, Preparation, characterisation and biological evaluation of biopolymer-coated multi-walled carbon nanotubes for sustained-delivery of silibinin, *Sci. Rep.*, 2020, **10**(1), 16941, DOI: 10.1038/s41598-020-73963-8.

40 N. Dlamini, H. Mukaya, R. Van Zyl, C. Chen, R. Zeevaart and X. Mbianda, Synthesis, characterization, kinetic drug release and anticancer activity of bisphosphonates multi-walled carbon nanotube conjugates, *Mater. Sci. Eng., C*, 2019, **104**, 109967.

41 J.-Y. Park, J.-S. Hyun, J.-G. Jee, S. J. Park and D. Khang, Structural deformation of MTX induced by nanodrug conjugation dictate intracellular drug transport and drug efficacy, *Int. J. Nanomed.*, 2021, 4943–4957.

42 N. Srivastava, V. Mishra, Y. Mishra, *et al.*, Development and evaluation of a protease inhibitor antiretroviral drug-loaded carbon nanotube delivery system for enhanced efficacy in HIV treatment, *Int. J. Pharm.*, 2024, **650**, 123678.

43 A. Chandra and M. Singh, Biosynthesis of amino acid functionalized silver nanoparticles for potential catalytic and oxygen sensing applications, *Inorg. Chem. Front.*, 2018, **5**(1), 233–257.

44 M. Habibizadeh, K. Rostamizadeh, N. Dalali and A. Ramazani, Preparation and characterization of PEGylated multiwall carbon nanotubes as covalently conjugated and non-covalent drug carrier: a comparative study, *Mater. Sci. Eng., C*, 2017, **74**, 1–9.

45 Z. Liu, Y. Jia, C. Wang, *et al.*, Organic anion transporters 1 (OAT1) and OAT3 meditated the protective effect of rhein on methotrexate-induced nephrotoxicity, *RSC Adv.*, 2017, **7**(41), 25461–25468.

46 A. Bce, S. Bozoğlu, N. Karatepe and F. S. Güner, Synthesis of Bovine Serum Albumin-Coated Magnetic Single-Walled Carbon Nanotubes as a Delivery System for Mitoxantrone, *ACS Omega*, 2025, **10**(1), 102–113.

47 N. K. Mehra and S. Palakurthi, Interactions between carbon nanotubes and bioactives: a drug delivery perspective, *Drug Discovery Today*, 2016, **21**(4), 585–597.

48 L. Wehl, C. von Schirnding, M. C. Bayer, O. Zhuzhgova, H. Engelke and T. Bein, Mesoporous Biodegradable Magnesium Phosphate-Citrate Nanocarriers Amplify Methotrexate Anticancer Activity in HeLa Cells, *Bioconjugate Chem.*, 2022, **33**(4), 566–575.

49 H. Majidzadeh, M. Araj-Khodaei, A. Aghanejad, *et al.*, PAMAM dendrimers based co-delivery of methotrexate and berberine for targeting of Hela cancer cells, *Toxicol Rep.*, 2024, **13**, 101765.

50 S. Uzuğ, O. Çetin, B. Aydın, Ç. İçhedef and S. Teksöz, *In vitro* evaluation of radiolabeled methotrexate loaded magnetic nanoparticle delivery system, *J. Radioanal. Nucl. Chem.*, 2023, **332**(11), 4745–4753.

51 S. Wu, X. Yang and X. Yang, Methotrexate and 10-hydroxycamptothecine loaded pullulan nanoparticles with the targeting property for efficient cancer therapy, *Mater. Technol.*, 2022, **37**(13), 2777–2784.

52 H. Singh, D. Dhar, S. Das and M. Halder, Methotrexate-loaded manganese nitrogen dual-doped carbon quantum dots as targeted nano drug-delivery system for potential use in cancer theranostics, *J. Photochem. Photobiol., A*, 2024, **455**, 115692.

53 E. Skverchinskaya, N. Levdarovich, A. Ivanov, I. Mindukshev and A. Bukatin, Anticancer drugs paclitaxel, carboplatin, doxorubicin, and cyclophosphamide alter the biophysical characteristics of red blood cells, *in vitro*, *Biology*, 2023, **12**(2), 230.

54 M. Thangavelu, A. Adithan, S. Thotapalli Parvathaleswara and C. Munusamy, Morphological modification of carbon nanoparticles after interacting with methotrexate as a potential anticancer agent, *Pharm. Res.*, 2018, **35**(10), 184.

55 B. Deepika, G. Janani, D. J. Mercy, *et al.*, Assessing the Anticancer Potential of Cerium Oxide Nanoparticles with Doxorubicin in a Polymeric Nanomatrix: Histopathological and Antiangiogenic Insights, *ChemNanoMat*, 2025, **11**(9), e202500186.

56 G. Janani, A. Girigoswami, B. Deepika, S. Udayakumar, D. J. Mercy and K. Girigoswami, Harnessing the anticancer potential of Amphiroa anceps: Folic acid-based liposomal nanocarriers for cancer cell killing *in vitro*, *Nanomedicine*, 2026, 102901.

57 L. Tang, Q. Xiao, Y. Mei, *et al.*, Insights on functionalized carbon nanotubes for cancer theranostics, *J. Nanobiotechnol.*, 2021, **19**(1), 423.

58 J. L. de la Fuente-Jiménez, C. I. Rodríguez-Rivas, I. B. Mitre-Aguilar, *et al.*, A Comparative and critical analysis for *in vitro* cytotoxic evaluation of magneto-crystalline zinc ferrite nanoparticles using mtt, crystal violet, ldh, and apoptosis assay, *Int. J. Mol. Sci.*, 2023, **24**(16), 12860.

59 N. Rani, K. Rawat, M. Saini, *et al.*, Comparative *in vitro* anticancer study of cisplatin drug with green synthesized ZnO nanoparticles on cervical squamous carcinoma (SiHa) cell lines, *ACS Omega*, 2023, **8**(16), 14509–14519.

60 D. Luo, X. Zeng, S. Zhang, *et al.*, Pirfenidone suppressed triple-negative breast cancer metastasis by inhibiting the activity of the TGF-β/SMAD pathway, *J. Cell. Mol. Med.*, 2023, **27**(3), 456–469.

61 K.-H. Jung, J. H. Lee, J. W. Park, *et al.*, Resveratrol-loaded polymeric nanoparticles suppress glucose metabolism and tumor growth *in vitro* and *in vivo*, *Int. J. Pharm.*, 2015, **478**(1), 251–257.

62 P. Gupta, S. Singh, N. Rai, *et al.*, Unveiling the cytotoxic and anti-proliferative potential of green-synthesized silver nanoparticles mediated by *Colletotrichum gloeosporioides*, *RSC Adv.*, 2024, **14**(6), 4074–4088.

63 E. Florek, M. Witkowska, M. Szukalska, *et al.*, Oxidative stress in long-term exposure to multi-walled carbon nanotubes in male rats, *Antioxidants*, 2023, **12**(2), 464.

64 M. Al-zharani, N. M. Alyami, A. A. Qurtam, *et al.*, Use of multi-walled carbon nanotubes (MWCNTs) stabilized in Arabic gum colloidal solution to induce genotoxicity and apoptosis of human breast and lung cancer cell lines, *Front. Mater.*, 2023, **10**, 1229637.

65 Z. Vafaiyan, R. Gharaei and J. Asadi, The correlation between telomerase activity and Bax/Bcl-2 ratio in valproic acid-treated MCF-7 breast cancer cell line, *Iran. J. Basic Med. Sci.*, 2015, **18**(7), 700.